Cancer Science
The official journal of the Japanese Cancer Association

Dual functional octreotide-modified liposomal irinotecan leads to high therapeutic efficacy for medullary thyroid carcinoma xenografts

Yuko Iwase and Yoshie Maitani[1]

Institute of Medicinal Chemistry, Hoshi University, Tokyo, Japan

(Received June 2, 2011/Revised September 16, 2011/Accepted October 18, 2011/Accepted manuscript online October 24, 2011)

Medullary thyroid carcinoma is a rare endocrine tumor, which shows overexpression of somatostatin receptor subtype 2. There is no systemic therapy for medullary thyroid carcinoma. Previously we reported that octreotide-PEG liposomes loaded with irinotecan, which target somatostatin receptor subtype 2, showed high therapeutic efficacy for medullary thyroid carcinoma xenografts compared with free irinotecan or non-targeted non-PEGylated liposomal irinotecan. In this study, we evaluated octreotide-PEG liposomes loaded with irinotecan in terms of the biodistribution of irinotecan and its active metabolite, and its therapeutic efficacy, compared with PEGylated liposomes. Furthermore, to elucidate the effect of octreotide ligand after cellular association, we assessed the cytotoxicity in tumor cells and the inhibition of protein phosphorylation in the tumor cells and xenografts using empty octreotide-PEG liposomes, which were loaded with no drug. In a therapeutic study, octreotide-PEG liposomes loaded with irinotecan significantly improved median survival compared with PEGylated liposomes. In tumor tissue at 6 h after injection, octreotide-PEG liposome-treated mice showed significantly higher concentrations of irinotecan and 7-ethyl-10-hydrocamptothecin compared with PEGylated liposome-treated mice, indicating that octreotide-PEG liposomes accumulated rapidly and to a high level in the tumor. Furthermore, empty octreotide-PEG liposome inhibited the phosphorylation of p70S6K *in vitro* and *in vivo*. These findings indicated that octreotide-PEG liposomal irinotecan has dual functions with targeted tumor delivery and assistance of cellular cytotoxicity, which led to higher therapeutic efficacy than PEGylated liposomes for medullary thyroid carcinoma xenografts. (*Cancer Sci*, doi: 10.1111/j.1349-7006.2011.02128.x, 2011)

Medullary thyroid carcinoma (MTC) originates in C cells of the thyroid gland. It is known to overexpress somatostatin receptor (SSTR) subtypes 1, 2, and 5.[1] Somatostatin receptor 2 expression was the most frequently detected subtype in human MTC and was significantly higher than the other SSTR subtypes in an established human MTC cell line, TT.[1–3] A therapeutic approach for MTC using irinotecan (CPT-11) was reported, but the results were inconclusive.[4,5] Overall, there is no systemic therapy for MTC.

CPT-11 is a water-soluble prodrug and is converted to 7-ethyl-10-hydrocamptothecin (SN-38), an active metabolite of CPT-11, by carboxylesterase (CE).[6,7] CPT-11 inhibits the resealing of single-strand DNA breaks mediated by topoisomerase I by stabilizing cleavable complexes and is a cell cycle-specific drug.[8–11] From this, a long period of exposure to CPT-11 induces cytotoxicity of tumor cells. The CPT-11 therapy, however, has failed owing to its short half-life and low tumor distribution. Therefore, selective delivery of CPT-11 to tumor sites could lead to successful CPT-11 therapy for MTC. For this purpose, we developed Oct-CL, namely, octreotide-PEG liposomes loaded with CPT-11, in which octreotide (Oct) has high binding affinity for SSTR2.[12] This approach proved promising because Oct-CL led to higher therapeutic efficacy for MTC xenografts than free CPT-11 or non-targeted non-PEGylated liposomal CPT-11.[13]

PEGylated liposomes (SL) can passively accumulate into tumor tissue due to the enhanced permeability and retention effect.[14] Therefore, we compared the therapeutic efficacy of antitumor activity of Oct-CL with SL to clarify whether the active-targeting ability of Oct-CL was superior to the passive-targeting ability of SL. Generally, because active-targeting liposome biodistribution is different from that of passive-targeting liposomes, we examined the biodistribution of CPT-11 and SN-38 after i.v. injection of Oct-CL and SL into MTC xenograft mice.

Moreover, we found that non-loaded Oct-CL, or empty Oct-CL, showed higher cytotoxicity in TT cells compared with empty SL.[13] To gain more insight into tumor suppression, we examined the mechanism of cytotoxicity of the Oct ligand. It was reported that Oct alone can produce an antiproliferative action to inhibit the phosphorylation of p70S6K in the Akt/mTOR/p70S6K pathway in insulinoma cells.[15] From this information, we tried to clarify the effects of Oct ligand on the phosphorylation of p70S6K *in vitro* and *in vivo*. We provide an answer to the mechanism of cytotoxicity of empty Oct-CL in this study.

Here we present a more extensive investigation of Oct-CL. We evaluated the function of Oct using Oct-CL from viewpoints of therapeutic efficacy and the biodistribution of CPT-11 and SN-38 in MTC tumor xenografts after injection of Oct-CL or SL. Furthermore, we assessed the cytotoxicity mechanism of Oct ligand using empty Oct-CL *in vitro* and *in vivo*.

Materials and Methods

Materials. CPT-11 was a kind gift from Yakult (Tokyo, Japan). Distearoylphosphatidylcholine (DSPC) and methoxy-PEG_{2000}-distearoylphosphatidylethanolamine (PEG-DSPE) were purchased from NOF (Tokyo, Japan). Oct-PEG_{3400}-DSPE[16] was purchased from KNC Laboratories (Kobe, Japan). SN-38 and cholesterol were purchased from Wako Pure Chemical Industries (Osaka, Japan). Phytic acid (IP-6) solution was obtained from Nacalai Tesque (Kyoto, Japan). Other reagents were of analytical or HPLC grade.

Preparation of liposomal CPT-11. Liposomal IP6 was prepared from DSPC/cholesterol at a molar ratio of 55/45, as reported previously.[13] Extra IP6 solution of liposomal IP6 was then exchanged for HBS-buffer (20 mM HEPES, 150 mM NaCl, pH 7.4) using a Sephadex G-50 column. The liposomal IP6 was loaded with CPT-11 aqueous solution at 60°C for 1 h. It was

[1]To whom correspondence should be addressed. E-mail: yoshie@hoshi.ac.jp

doi: 10.1111/j.1349-7006.2011.02128.x

then incubated with 1.6 mol% Oct-PEG-DSPE for Oct-CL or 1.6 mol% PEG-DSPE for SL at 60°C for 25 min.[13] Empty liposomes were prepared using the same protocol but without loading drug. The particle size and zeta-potential were measured using an ELS-Z2 (Otsuka Electronics, Osaka, Japan) at 25 ± 1°C after diluting the liposome suspension in water.

Cytotoxicity assay on TT cells. Cytotoxicity on TT cells (human MTC cell line) was carried out using free Oct or empty liposomes. The Oct concentration of empty Oct-CL was measured by an Oct-EIA kit (Peninsula Laboratories, LLC, San Carlos, CA, USA). Cells were incubated for 48 h at the different concentrations of free Oct, empty liposomes in the presence or absence of 1.5 μM CPT-11, which corresponded to one-tenth of the 50% growth-inhibitory concentration.[13] The lipid amount of empty SL corresponded to that of empty Oct-CL. Cell viability was measured by a cell proliferation kit (Dojindo, Kumamoto, Japan) as reported previously.[13]

Animals. All animal experiments were carried out with approval from the Institutional Animal Care and Use Committee at Hoshi University (Tokyo, Japan). TT cells (1×10^7) were inoculated s.c. into female ICR nu/nu mice (6 weeks of age; Oriental Yeast, Tokyo, Japan).

Antitumor effects. When the average tumor volume was approximately 100 mm^3, Oct-CL or SL was injected i.v. at a dose of 10 mg CPT-11/kg in two injections at 3-day intervals (23.9 mg lipid/kg/injection). Empty Oct-CL or empty SL was injected i.v. (23.5 mg lipid and 867 nmol Oct/kg/injection, corresponding to Oct ligand amount for the therapeutic study) in two injections at 3-day intervals. Tumor volume and body weight were measured for individual animals. Tumor volume was calculated using the following equation: volume = $1/2ab^2$, where a is the long diameter and b is a short diameter.

Biodistribution in TT xenograft mice by HPLC. When the average tumor size reached approximately 100 mm^3, mice were treated with Oct-CL or SL i.v. at a dose of 10 mg CPT-11/kg. At 6 h and 24 h after a single injection, blood was collected. Tumor, liver, kidneys, lung, and spleen were excised and homogenized. CPT-11 and SN-38 were extracted using ice-cold acidic methanol and analyzed by HPLC methods, as reported previously.[17] The CPT-11 dose %/mL plasma or g tissue was calculated as the amount of CPT-11 per total plasma volume (mL) or per total tissue weight (g), respectively, from that of injected liposomal CPT-11.[17]

Distribution of liposomal CPT-11 in TT xenograft mice by fluorescence microscope. When the average tumor size reached approximately 150 mm^3, mice were treated with Oct-CL or SL i.v. at a dose of 10 mg CPT-11/kg. At 6 and 24 h after a single injection, tissues were collected and prepared as 20-μm frozen sections. Tissue sections were examined using an inverted microscope, ECRIPS TS100 (Nikon, Tokyo, Japan), with an Epi-Fluorescence Attachment (Nikon) using a UV1A filter.

Conversion activity of CPT-11 by CE. The conversion activity of CPT-11 by CE (CPT-CE activity) in TT cells, normal liver, and TT tumor tissue was measured by the Guichard method.[18] Briefly, TT cells (4×10^4 cells) were homogenized. The homogenates were centrifuged at 20 000 g for 30 min at 4°C to obtain cytosol. Cytosolic protein (3 mg/mL, 80 μL) and 5 μM CPT-11 (20 μL) were mixed and incubated at 37°C for 1 h. Then ice-cold acidic acetonitrile was added to stop the reaction. SN-38 produced during the incubation was measured by an HPLC method, as previously reported.[17] The TT tumor tissue and liver were excised and homogenized. Cytosol from the TT tumor tissue and normal liver, which was perfused with ice-cold saline to remove blood, was prepared using the same protocol as for the extraction protocol in TT cells. CPT-CE activity in normal liver and TT tumor tissue was measured using the same protocol as for the assay protocol in TT cells.

Effects of empty liposomes, CPT-11, or SN-38 on the PI3K/Akt/mTOR/p70S6K pathway in TT cells. TT cells were incubated with serum-starved (0.1% FBS) cell medium with empty Oct-CL, empty SL, CPT-11, or SN-38 for 24 h at 37°C. Cell lysates were prepared with ice-cold RIPA buffer (20 mM Tris-HCl (pH 7.5), 150 mM NaCl, 1% Triton X-100 containing protease and phosphatase inhibitors), separated by SDS-PAGE, and blotted using standard procedures.[19] Primary antibodies were against Akt, tuberous sclerosis complex 2, tuberin (TSC2), p70S6K, phosphorylated Akt (Ser473), phosphorylated TSC2 (Thr1462), and phosphorylated p70S6K (Thr389) (all made in rabbits; Cell Signaling Technology, Beverly, MA, USA). Horseradish peroxidase-conjugated secondary antibody was used to detect the primary rabbit antibody (Santa Cruz Biotechnology, Santa Cruz, CA, USA). All proteins were detected by peroxidase-induced chemiluminesence (Super Signal West Pico Chemiluminescent substrate; Pierce, Rockford, IL, USA).

Effects of empty liposomes on the PI3K/Akt/mTOR/p70S6K pathway in TT tumors. When the average tumor size reached approximately 150 mm^3, empty Oct-CL or empty SL was injected i.v. once (23.5 mg lipid and 867 nmol Oct/kg). At 24 h after injection, tumor tissue was collected and homogenized in RIPA buffer. Western blot analysis was carried out using the same protocol as for the *in vitro* study.

Statistical analysis. The statistical significance of differences in the data was evaluated by analysis using one-way ANOVA in combination with the Tukey–Kramer test. $^{*}P < 0.05$ and $^{**}P < 0.01$ were considered significant. Kaplan–Meier analysis was carried out using GraphPad Prism version 4.0 (GraphPad Software, San Diego, CA, USA).

Results

Size and zeta-potential of liposomes. Two types of liposomes, 1.6 mol% Oct-PEG-DSPE modified Oct-CL and 1.6 mol% PEG-DSPE modified SL were prepared (Table 1), because we reported previously that 1.6 mol% Oct modification was effective for association with TT cells.[13] The average particle size of each liposome was ~146 nm with a narrow monodisperse distribution. The zeta-potential and drug entrapment efficiency of each liposome formulation was approximately −14 mV and >80%, respectively. There were no significant differences between Oct-CL and SL in terms of particle characters such as particle size, zeta-potential, or drug entrapment efficiency, except for active-targeting ability.

Therapeutic efficacy of liposomal CPT-11. The antitumor effect of Oct-CL and SL was evaluated in TT tumor xenografts. Oct-CL showed significantly stronger antitumor effects at days 7–25 after the treatment compared with saline and at days 7–15 compared with SL (Fig. 1a). Body weight losses were not observed (Fig. 1b). Oct-CL treatment significantly improved median survival up to 212 days, compared with 198 and 121 days observed in the SL-treated group ($P < 0.01$) and saline-treated group ($P < 0.05$), respectively (Fig. 1c).

Table 1. Particle size and zeta-potential of liposomal CPT-11

Formulation	Size (nm)	Zeta-potential (mV)
Oct-CL	146.9 ± 20.1	−14.0 ± 1.3
SL	146.2 ± 15.0	−13.4 ± 0.9

Values represent the mean ± SD (n = 3). Oct-CL, non-PEGylated liposomes modified with 1.6 mol% octreotide-methoxy-PEG_{3400}-distearoylphosphatidylethanolamine; SL, PEGylated liposomes modified with 1.6 mol% methoxy-PEG_{2000}-distearoylphosphatidylethanolamine.

doi: 10.1111/j.1349-7006.2011.02128.x

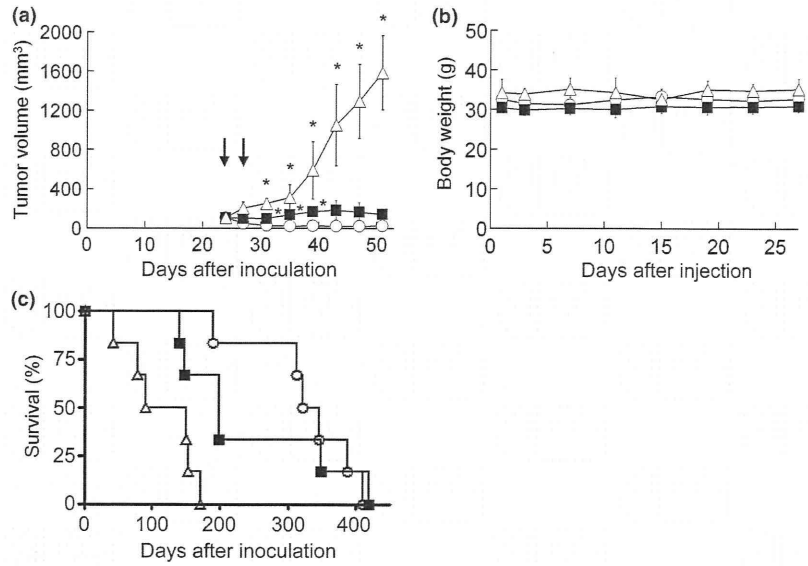

Fig. 1. Therapeutic efficacy of treatment for medullary thyroid carcinoma using octreotide-PEG liposomes (Oct-CL) or PEGylated liposomes (SL). Mice were injected i.v. with Oct-CL (○), SL (■) (equivalent to 10 mg CPT-11/kg), or saline (Δ), as shown by arrows. Their treatment effects on tumor size (a), body weight (b), and survival rate (c) were measured. Each value represents the mean ± SD (n = 6). *P < 0.05 versus Oct-CL-treated mice.

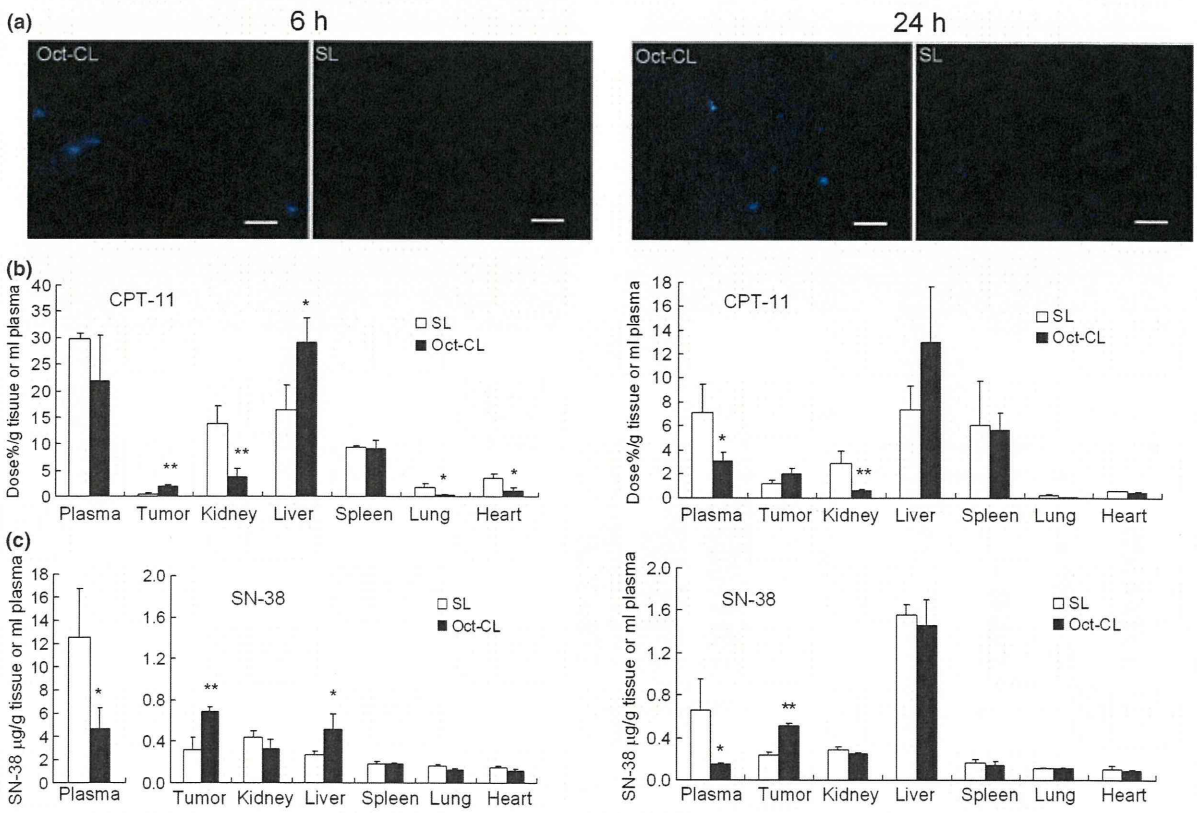

Fig. 2. Biodistribution of liposomal CPT-11 (Oct-CL) at 6 or 24 h after a single injection into mice. Frozen sections of tumors were observed using a fluorescence microscope (a), and tissue biodistribution of CPT-11 (b) and SN-38 (c). Each value represents the mean ± SD (n = 3). *P < 0.05 and **P < 0.01 versus PEGylated liposomes (SL). Blue fluorescence indicates CPT-11. Scale bars = 100 μm.

Biodistribution of liposomal CPT-11. The biodistribution of CPT-11 and SN-38 was examined in TT xenografts at 6 or 24 h after i.v. injections of Oct-CL or SL loaded with CPT-11. CPT-11 was highly distributed in the liver and spleen (Fig. 2). Frozen sections of tumors in the Oct-CL treated group were observed with blue fluorescence of CPT-11 than those in SL treated group, both 6 and 24 h after injection (Fig. 2a). SN-38 was not able to be detected under this condition. CPT-11 blue

fluorescence was weak and was not enough to show significant difference in CPT-11 tumor accumulation between Oct-CL- and SL-treated groups. Therefore, we next measured concentrations of CPT-11 and SN-38 in tumor tissues and other organs by the HPLC method. Six hours after injection, CPT-11 levels in the liver of Oct-CL-treated mice were significantly higher than that of SL-treated mice ($P < 0.05$) (Fig. 2b). CPT-11 and SN-38 levels in tumor tissue of Oct-CL-treated mice were significantly higher, 3.7- and 2-fold, respectively, compared with that of SL-treated mice ($P < 0.01$) (Fig. 2b,c). However, the kidney distribution of CPT-11 in Oct-CL-treated mice was significantly lower than that of SL-treated mice ($P < 0.01$). Twenty-four hours after injection, SL-treated mice maintained a higher CPT-11 level in the plasma (7.1 ± 2.4% dose/mL), whereas Oct-CL-treated mice showed approximately half the CPT-11 plasma concentration of SL-treated mice ($P < 0.05$). Tumor CPT-11 concentration between the Oct-CL- and SL-treated groups was not significantly different, but the SN-38 concentration in the Oct-CL-treated group was significantly higher, 2.2-fold, than in SL-treated mice ($P < 0.01$).

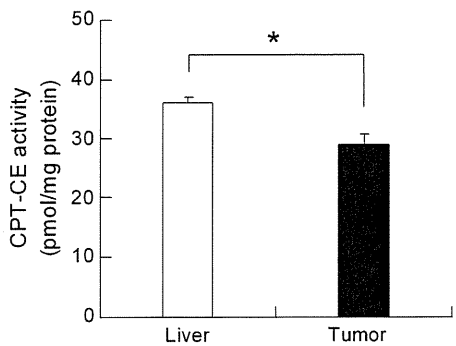

Fig. 3. CPT-11 converted by carboxylesterase (CE) activity. Cytosol was incubated with CPT-11 at 37°C for 1 h. Each value represents the mean ± SD ($n = 3$). *$P < 0.05$.

In other organs, the results of the biodistribution of CPT-11 measured by HPLC agreed with the observation of blue fluorescence of CPT-11 (Fig. S1).

***In vitro* conversion of CPT-11 to SN-38 in TT cells, liver, and TT tumor tissues.** In the biodistribution study, higher SN-38 accumulation was observed in tumor tissues 6 and 24 h after injection of Oct-CL compared to SL. To confirm the conversion of CPT-11 to SN-38 in TT cells, we analyzed the *in vitro* conversion of CPT-11 to SN-38 in TT cells. The cytosol of TT cells showed the conversion of CPT-11 to SN-38 at a rate of 2.53 ± 0.09 pmol/h/mg protein (data not shown). TT cells *per se* have the conversion activity of CPT-11 to SN-38. With regard to TT tumor tissue, the conversion rate in the liver was approximately 8.5% of the CPT-11 that was initially added to the reaction mixture (100 pmol CPT-11) (Fig. 3). Interestingly, the conversion of CPT-11 to SN-38 activity in TT tumor tissue was 0.8-fold that of the liver, suggesting that CPT-11 loaded into Oct-CL was accumulated in the tumor directly by active targeting of Oct-CL, and was converted into SN-38. The negative control (initially adding the stop solution before the addition of CPT-11 and incubation) showed no production of SN-38.

Effects of Oct ligand of liposomes on growth inhibition and phosphorylation of p70S6K. As shown in Figure 4(a), empty Oct-CL exerted a growth inhibitory effect on TT cells in a dose-dependent fashion of Oct ligand. Furthermore, addition of 1.5 μM CPT-11 potentiated the growth inhibition activity of empty Oct-CL, having led to an additional ~20% reduction in cell viability. In contrast, empty SL did not exert any growth inhibitory effect in the presence or absence of CPT-11 (Fig. 4b). Free Oct showed a growth inhibitory effect only at high concentration, 100 μM (Fig. 4c), but showed no synergistic effect with CPT-11.

In many cancers, the PI3K/Akt/mTOR pathway contributes to cell proliferation and growth, and this pathway is activated by phosphorylation of Akt, TSC2, or p70S6K proteins.[12,20–25] Therefore, we tried to clarify the effects of Oct ligand on

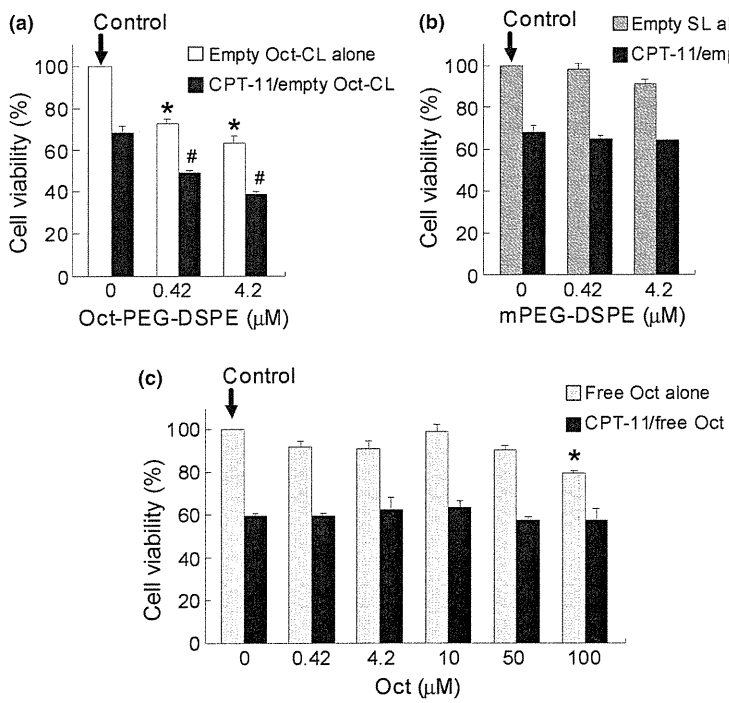

Fig. 4. Cytotoxicity of free octreotide (Oct) or empty liposomes on human medullary thyroid carcinoma TT cells in the presence or absence of CPT-11. The TT cells were treated with empty octreotide-PEG liposomes (Oct-CL) (a), empty PEGylated liposomes (SL) (b), or free Oct (c), alone or combined with CPT-11. Each value represents the mean ± SD ($n = 4$). DSPE, distearoylphosphatidylethanolamine. *$P < 0.05$ versus control (cell viability of non-treatment); #$P < 0.05$ versus CPT-11 alone.

doi: 10.1111/j.1349-7006.2011.02128.x

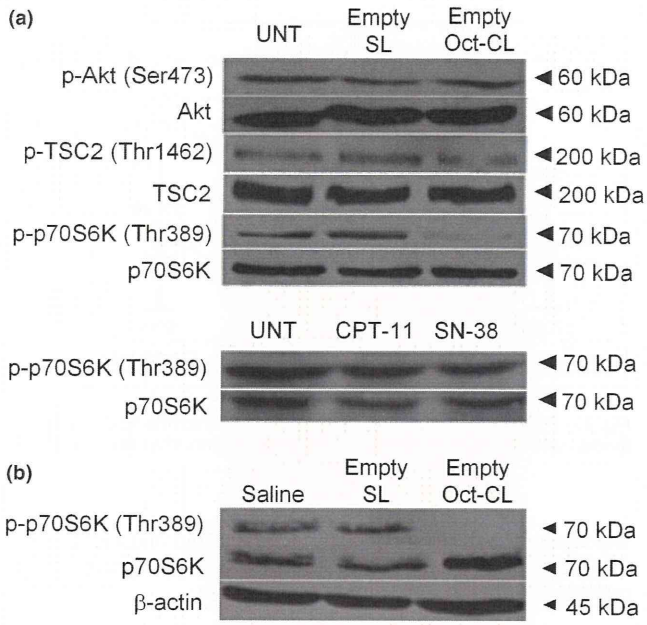

Fig. 5. Effects of empty PEGylated liposomes (SL) or empty octreotide-PEG liposomes (Oct-CL) on Akt-TSC2-p70S6K in human medullary thyroid carcinoma TT cells (a) and TT tumor tissue (b). TT cells were treated with empty Oct-CL (corresponding to 0.42 μM Oct-PEG-distearoylphosphatidylethanolamine [DSPE]), empty SL liposomes modified with 0.42 μM PEG-DSPE, CPT-11 (13 μM), or SN-38 (0.14 μM) for 24 h. TT tumor-bearing mice were injected with empty Oct-CL 24 h before the experiment. UNT, untreated.

phosphorylation of proteins in TT cells and TT tumors by Western blotting, using empty Oct-CL, empty SL, CPT-11, or SN-38. As shown in Figure 5(a), empty SL and empty Oct-CL did not affect the phosphorylation of either Akt or TSC2 in TT cells. Only empty Oct-CL (corresponding to 0.42 μM Oct ligand) strongly inhibited the phosphorylation of p70S6K at the Thr389 site, whereas total p70S6K was not affected. In TT tumor tissue, empty Oct-CL or empty SL did not affect total protein p70S6K. Mice injected with empty Oct-CL showed a decrease in the level of phosphorylated p70S6K, but those with empty SL did not (Fig. 5b). However, the empty Oct-CL and the empty SL did not show antitumor effects under this experiment condition in TT tumor xenografts (Fig. 6).

Discussion

In this study, we showed that Oct-CL loaded with CPT-11 showed the early and higher accumulation of CPT-11 in tumor, enhanced the antitumor effect, and significantly prolonged median survival compared with SL. Moreover, the mechanism of action of Oct associated with liposomes was investigated by measuring the biodistribution of Oct-CL loaded with CPT-11 and the phosphorylation of proteins after empty Oct-CL treatment. Recently, we have reported that Oct-CL loaded with CPT-11 showed higher therapeutic efficacy compared with free CPT-11 or non-targeted non-PEGylated liposome in TT tumor xenografts.[13] However, the effect of Oct and its mechanism still remained after association with liposomes.

In our study, Oct-CL showed a significantly higher distribution to TT tumor tissue compared with SL at least until 6 h after injection. This result suggested that Oct-CL accumulated rapidly in the tumor after injection as a result of Oct-targeting, whereas SL accumulated slowly in the tumor by the enhanced permeability and retention effect for 24 h. Twenty-four hours after injection, there was no significant difference between Oct-CL and SL. The CPT-11 level of Oct-CL in the tumor was sustained for 24 h after injection.

Why was the SN-38 concentration of tumors in Oct-CL-treated mice significantly higher than that of SL-treated mice at 24 h even though the CPT-11 concentration was similar? Generally, it is reported that CPT-11 conversion to SN-38 mainly occurs through the action of liver CE.[26] Accordingly, it can be regarded that SN-38 transformed in the liver accumulated in the tumor. When the accumulation of CPT-11 in the liver was similar between Oct-CL- and SL-treated mice, converted SN-38 in the liver should be present in similar amounts, and, therefore, the amount of SN-38 accumulating in tumor should be similar. We previously reported that there were no significant differences between Oct-CL- and SL-treated mice in terms of drug release over 48 h at 37°C in PBS.[13] Furthermore, an *in vitro* conversion study showed that the conversion activity of CPT-11 to SN-38 in TT tumor tissue was 0.8-fold that of the liver. From these findings, higher SN-38 concentration of Oct-CL at 24 h might reflect early direct distribution of Oct-CL to tumor tissue by SSTR targeting. To the best of our knowledge, this is the first report regarding CPT-11 conversion activity in TT cells and TT tumor tissue.

When we examined other tissues, there were significant differences between Oct-CL- and SL-treated mice in terms of kidney and liver distribution. The CPT-11 concentration in the kidneys of Oct-CL-treated mice was significantly lower compared with that of SL-treated mice. Because the kidney is known to express SSTR2,[27] Oct-CL might be selectively and rapidly distributed to the kidneys, as well as to the tumor, then excreted more rapidly than in SL-treated mice. With regard to the liver, Oct-CL accumulated to a higher level in the liver than SL, because SL was modified with Oct ligand and it may be taken up by the reticuloendothelial system.

Empty Oct-CL exerted cell growth inhibition at low concentrations (0.42 and 4.2 μM), whereas free Oct did not exert cell growth inhibition below 100 μM (Fig. 4a,c). Empty Oct-CL showed effective cell growth inhibition compared with free Oct, suggesting that the affinity of empty Oct-CL to SSTR may be higher than that of free Oct. Phosphorylation of p70S6K is reported to activate cell growth and proliferation.[24] p70S6K is

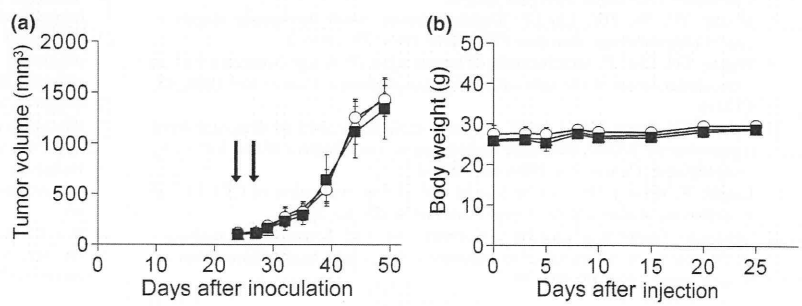

Fig. 6. Therapeutic efficacy of injection of empty octreotide-PEG liposomes (Oct-CL) or empty PEGylated liposomes (SL) into mice bearing human medullary thyroid tumors at a dose of 23.5 mg lipid and 867 nmol Oct/kg/injection or 23.5 mg lipid, respectively. Treatment effects of empty liposomes on tumor size (a) and body weight (b) were measured. The formulations used were empty Oct-CL (○), empty SL (■), and saline (Δ). Each value represents the mean ± SD (n = 6). Arrows indicated the day of drug injection.

the downstream protein of the PI3K/Akt/mTOR pathway and phosphorylation of p70S6K is generally used as a marker of the inhibition of the PI3K/Akt/mTOR pathway.[28] Treatment with empty Oct-CL caused the suppression of phosphorylation of p70S6K *in vitro* and *in vivo* (Fig. 5a,b) but empty SL did not. Therefore, this result suggested that empty Oct-CL inhibited cell growth and proliferation by suppressing the phosphorylation of p70S6K in TT cells and TT tumor tissue. In other words, the targeting ligand Oct had not only tumor targeting activity but also assisted with antitumor effects. Therefore, the Oct ligand has dual functionality.

However, treatment with empty Oct-CL did not show any antitumor effect under this condition (Fig. 6). For MTC, it was reported that clinically s.c. injection of free Oct at 500 μg (=458 nmol)/day for 90 days, and 150 μg (=137 nmol)/day for 6 months showed no effect on therapeutic efficacy.[29,30] In this therapeutic study, Oct originated from Oct-CL was injected twice as 867 nmol Oct/kg/day. From these different schedules, it is difficult to judge the therapeutic efficacy by Oct alone in our study.

Figure 7 illustrates the proposed antitumor effects of Oct-CL loaded with CPT-11 for MTC. Oct-CL was selectively associated with TT cells. CPT-11 was released from Oct-CL, then CPT-11 was converted to SN-38 by CE in TT tumor. SN-38 produced in the tumors showed cytotoxicity. Oct-CL suppressed the phosphorylation of p70S6K. These suppressions led to inhibition of cell growth and proliferation, which assisted in antitumor effects for MTC using Oct-CL loaded with CPT-11.

In conclusion, the present study showed that Oct-CL loaded with CPT-11 showed enhanced therapeutic efficacy, which correlated with a strong antitumor effect and the significant improvement of median survival, which was superior to SL in TT tumor xenografts. The improvement in therapeutic efficacy was due to the dual functions of Oct; the rapid and highly selective distribution of Oct-CL to tumor by SSTR targeting and the assistance of cell growth suppression by Oct.

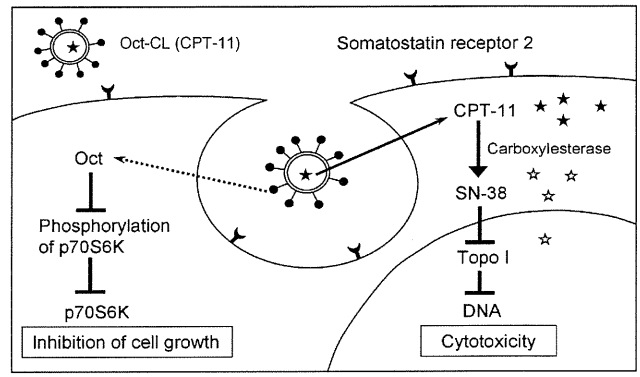

Fig. 7. Proposed antitumor effects of octreotide-PEG liposomes loaded with CPT-11 (Oct-CL) for human medullary thyroid carcinoma.

Acknowledgments

This study was supported in part by the Ministry of Education, Culture, Sports, Science and Technology of Japan and by the Open Research Center Project.

Disclosure Statement

The authors have no conflict of interest.

References

1 Zatelli MC, Tagliati F, Taylor JE *et al.* Somatostatin receptor subtypes 2 and 5 differentially affect proliferation *in vitro* of the human medullary thyroid carcinoma cell line TT. *J Clin Endocrinol Metab* 2001; **86**: 2161–9.
2 Zatelli MC, Tagliati F, Taylor JE *et al.* Somatostatin, but not somatostatin receptor subtypes 2 and 5 selective agonists, inhibits calcitonin secretion and gene expression in the human medullary thyroid carcinoma cell line, TT. *Horm Metab Res* 2002; **5**: 229–33.
3 Mato E, Matias-Guiu X, Chico A *et al.* Somatostatin and somatostatin receptor subtype gene expression in medullary thyroid carcinoma. *J Clini Endocrinol Metab* 1998; **83**: 2417–20.
4 Strock CJ, Park JI, Rosen DM *et al.* Activity of irinotecan and the tyrosine kinase inhibitor CEP-751 in medullary thyroid cancer. *J Clin Endocrinol Metab* 2006; **91**: 79–84.
5 Koga K, Hattori Y, Komori M *et al.* Combination of RET siRNA and irinotecan inhibited the growth of medullary thyroid carcinoma TT cells and xenografts *via* apoptosis. *Cancer Sci* 2010; **101**: 941–7.
6 Kawato Y, Aonuma M, Hirota Y *et al.* Intracellular roles of SN-38, a metabolite of the camptothecin derivative CPT-11, in the antitumor effect of CPT-11. *Cancer Res* 1991; **51**: 4187–91.
7 Kawato Y, Furuta T, Aonuma M *et al.* Antitumor activity of a camptothecin derivative, CPT-11, against human tumor xenografts in nude mice. *Cancer Chemother Pharmacol* 1991; **28**: 192–8.
8 Hsiang YH, Wu HY, Liu LF. Topoisomerases: novel therapeutic targets in cancer chemotherapy. *Biochem Pharmacol* 1988; **37**: 1801–2.
9 Hsiang YH, Liu LF. Identification of mammalian DNA topoisomerase I as an intracellular target of the anticancer drug camptothecin. *Cancer Res* 1988; **48**: 1722–6.
10 Hsiang YH, Lihou MG, Liu LF. Arrest of replication forks by drug-stabilized topoisomerase I–DNA cleavable complexes as a mechanism of cell killing by camptothecin. *Cancer Res* 1989; **49**: 5077–82.
11 Lavelle F, Bissery MC, Andre S *et al.* Preclinical evaluation of CPT-11 and its active metabolite SN-38. *Semin Oncol* 1996; **23**: 11–20.
12 Grozinsky-Glasberg S, Shimon I, Korbonits M *et al.* Somatostatin analogues in the control of neuroendocrine tumours: efficacy and mechanisms. *Endocr-Relat Cancer* 2008; **15**: 701–20.
13 Iwase Y, Maitani Y. Octreotide-targeted liposomes loaded with CPT-11 enhanced cytotoxicity for the treatment of medullary thyroid carcinoma. *Mol Pharm* 2011; **8**: 330–7.
14 Matsumura Y, Maeda HA. New concept for macromolecular therapeutics in cancer chemotherapy mechanism of tumoritropic accumulation of proteins and the antitumor agent smancs. *Cancer Res* 1986; **46**: 6387–92.
15 Grozinsky-Glasberg S, Franchi G, Teng M *et al.* Octreotide and the mTOR inhibitor RAD001 (Everolimus) block proliferation and interact with the Akt-mTOR-p70S6K pathway in a neuro-endocrine tumor cell line. *Neuroendocrinolgy* 2008; **87**: 168–81.
16 Su JC, Tseng CL, Chang TG *et al.* A synthetic method for peptide-PEG-lipid conjugates: application of Octreotide-PEG-DSPE synthesis. *Bioorg Med Chem Let* 2008; **18**: 4593–6.
17 Hattori Y, Shi L, Ding W *et al.* Novel irinotecan-loaded liposome using phytic acid with high therapeutic efficacy for colon tumors. *J Control Release* 2009; **136**: 30–7.
18 Guichard S, Terret C, Hennebelle I *et al.* CPT-11 converting carboxylesterase and topoisomerase activities in tumour and normal colon and liver tissues. *Br J Cancer* 1999; **80**: 364–70.
19 Hattori Y, Yoshizawa T, Koga K *et al.* NaCl induced high cationic hydroxyethylated cholesterol-based nanoparticle-mediated synthetic small interfering RNA transfer into prostate carcinoma PC-3 cells. *Biol Pharm Bull* 2008; **31**: 2294–301.
20 Altomare DA, Testa JR. Perturbations of the AKT signaling pathway in human cancer. *Oncogene* 2005; **24**: 7455–64.
21 Cheng JQ, Ruggeri B, Klein WM *et al.* Amplification of AKT2 in human pancreatic cells and inhibition of AKT2 expression and tumorigenicity by antisense RNA. *Proc Natl Acad Sci USA* 1996; **93**: 3636–41.
22 Vasko V, Saji M, Hardy E *et al.* Akt activation and localisation correlate with tumour invasion and oncogene expression in thyroid cancer. *J Med Genet* 2004; **41**: 161–70.
23 Bellacosa A, Kumar CC, Di Cristofano A *et al.* Activation of AKT kinases in cancer: implications for therapeutic targeting. *Adv Cancer Res* 2005; **94**: 29–86.
24 Wu C, Huang J. Phosphatidylinositol 3-kinase-AKT-mammalian target of rapamycin pathway is essential for neuroendocrine differentiation of prostate cancer. *J Biol Chem* 2007; **282**: 3571–83.

doi: 10.1111/j.1349-7006.2011.02128.x

25 McManus EJ, Alessi DR. TSC1–TSC2: a complex tale of PKB-mediated S6K regulation. *Nature Cell Biol* 2002; **4**: E214–16.
26 Rivory LP, Bowles MR, Robert J *et al.* Conversion of irinotecan (CPT-11) to its active metabolite, 7-ethyl-10-hydroxycamptothecin (SN-38), by human liver carboxylesterase. *Biochem Pharmacol* 1996; **52**: 1103–11.
27 Lamberts SWJ, Lery AJ, Herder WW *et al.* Octreotide. *Drug Therapy* 1996; **334**: 246–54.
28 Boulay A, Zumstein-Mecker S, Stephan C *et al.* Antitumor efficacy of intermittent treatment schedules with the rapamycin derivative RAD001 correlates with prolonged inactivation of ribosomal protein S6 kinase 1 in peripheral blood mononuclear cells. *Cancer Res* 2004; **64**: 252–61.
29 Modigliani E, Cohen R, Joannidis S *et al.* Results of long-term continuous subcutaneous octreotide administration in 14 patients with medullary thyroid carcinoma. *Clin Endocrinol* 1992; **36**: 183–6.
30 Lupoli G, Cascone E, Arlotta F *et al.* Treatment of advanced medullary thyroid carcinoma with a combination of recombinant interferon alpha-2b and octreotide. *Cancer* 1996; **78**: 1114–8.

Supporting Information

Additional Supporting Information may be found in the online version of this article:

Fig. S1. Distribution of liposomal CPT-11 in the liver, spleen, lung, and kidneys.

Please note: Wiley-Blackwell are not responsible for the content or functionality of any supporting materials supplied by the authors. Any queries (other than missing material) should be directed to the corresponding author for the article.

Pharm Res (2012) 29:178–186
DOI 10.1007/s11095-011-0525-3

RESEARCH PAPER

Tumor Environment Changed by Combretastatin Derivative (Cderiv) Pretreatment That Leads to Effective Tumor Targeting, MRI Studies, and Antitumor Activity of Polymeric Micelle Carrier Systems

Kouichi Shiraishi • Yoshiko Harada • Kumi Kawano • Yoshie Maitani • Katsuyoshi Hori • Kazuyoshi Yanagihara • Misato Takigahira • Masayuki Yokoyama

Received: 28 April 2011 / Accepted: 29 June 2011 / Published online: 26 July 2011

ABSTRACT

Purpose To evaluate effect of a vascular disrupting agent, a combretastatin derivative (Cderiv), on tumor targeting for polymeric micelle carrier systems, containing either a diagnostic MRI contrast agent or a therapeutic anticancer drug.

Methods Cderiv was pre-administered 72 h before polymeric micelle MRI contrast agent injection. Accumulation of the MRI contrast agent in colon 26 murine tumor was evaluated with or without pretreatment of Cderiv by ICP and MRI.

Results Significantly higher accumulation of the MRI contrast agent was found in tumor tissues when Cderiv was administered at 72 h before MRI contrast agent injection. T_1-weighted images of the tumor exhibited substantial signal enhancement in tumor area at 24 h after the contrast agent injection. In T_1-weighted images, remarkable T_1-signal enhancements were observed in part of tumor, not in whole tumor. These results indicate that Cderiv pretreatment considerably enhanced the permeability of the tumor blood vessels. Antitumor activity of adriamycin encapsulated polymeric micelles with the Cderiv pretreatment suppressed tumor growth in 44As3 human gastric scirrhous carcinoma-bearing nude mice.

Conclusions Pretreatment of Cderiv enhanced tumor permeability, resulting in higher accumulation of polymeric micelle carrier systems in solid tumors.

KEY WORDS Cderiv · MRI study · polymeric micelle MRI contrast agent · tumor permeability · tumor vascular disrupting agent

ABBREVIATIONS

ADR-micelle	adriamycin-encapsulating polymeric micelle
Cderiv	(Z)-N-[2-methoxy-5-[2-(3,4,5- trimethoxy-phenyl)vinyl] phenyl]-L-serinamide hydrochloride
DLS	dynamic light scattering

Y. Harada
Kanagawa Academy of Science and Technology
Yokoyama "Nano-medical Polymer" Project
KSP East 404, Sakado 3-2-1, Takatsu-ku
Kawasaki, Kanagawa 213-0012, Japan

K. Kawano • Y. Maitani
Institute of Medicinal Chemistry Hoshi University
2-4-41 Ebara, Shinagawa-ku, Tokyo 142-8501, Japan

K. Hori
Department of Vascular Biology, Division of Cancer Control
Institute of Development Aging and Cancer, Tohoku University
4-1 Seiryomachi, Aoba-ku, Sendai 980-8575, Japan

K. Yanagihara
Department of Life Sciences, Laboratory of Molecular Cell Biology
Yasuda Woman's University Faculty of Pharmacy
6-13-1 Yasuhigashi, Asaminami-ku, Hiroshima, 731-0153, Japan

M. Takigahira
Central Animal Laboratory
National Cancer Center Research Institute
5-1-1 Tsukiji, Chuo-ku, Tokyo 104-0045, Japan

M. Takigahira
Shien Laboratory National Cancer Center Hospital
Tokyo, Japan

K. Shiraishi • M. Yokoyama (✉)
Medical Engineering Laboratory, Research Center for Medical Science
The Jikei University School of Medicine
Nishi-shinbashi 3-25-8, Minato-ku, Tokyo 105-8461, Japan
e-mail: masajun2093ryo@jikei.ac.jp

DOTA	1,4,7,10-Tetraazacyclododecane-1,4,7, 10-tetraacetic acid
EDC	1-ethyl-3-(3-dimethylaminopropyl) carbodiimide hydrochloride
EPR effect	enhanced permeability and retention effect
GPC	gel permeation chromatography
ICP	inductive coupled plasma
MRI	magnetic resonance imaging
MWCO	molecular weight cut-off
PEG-P(Lys)	poly(ethylene glycol)-b-poly(L-lysine)
ROI	region of interest
TGF-β	transforming growth factor β
TR/TE	repetition time/echo time

INTRODUCTION

Nowadays, targeting potential anticancer drugs to solid tumors by means of nanocarriers is a promising tool to maximize anticancer activity. This entire strategy for tumor targeting is based on the enhanced permeability and retention (EPR) effect (1,2). It is a well-known phenomenon that solid tumors have leaky blood vessels, namely, macromolecules of more than 40 kDa show substantial extravasation from the leaky tumor blood vessels, resulting in a large amount of accumulation in solid tumors. Many researchers have focused on macromolecular drugs that have sizes in the nanometer region to develop selective tumor targeting through the EPR effect (3). Improvement of pharmacokinetics of poorly soluble anticancer drug by means of such nano-sized drug carriers achieved long-circulation of the drug in blood which is necessary for selective tumor targeting through the EPR effect. This selective drug targeting leads to improved chemotherapy of the anticancer drug and diminishes negative side effects.

A doxorubicin encapsulated in liposome covered with poly(ethylene glycol) on the surface was approved as Doxil for treatment of Kaposi sarcoma (4). Polymer therapeutics, such as polymer-drug conjugate and polymeric micelle carriers, have been developed (5,6).

However, in our recent study on transparent chambers and a vital microscopic systems, we obtained some additional knowledge about EPR-based targeting system (7). That study examined the permeability of FITC-labeled polymeric micelles at different tumor growth stages relative to Yoshida ascites sarcoma in LY80. The FITC-labeled polymeric micelle was distributed in vessels at the interface between normal and tumor tissues, and the interface between tumor tissues and necrotic areas. It was found that the polymeric micelle accumulated in necrotic areas with dysfunction of the circulatory system. The study showed that the polymeric micelle was not accumulated in 1 mm of the microtumor without necrotic areas. This observation indicates that the tumor blood vessels in microtumors did not leak nanocarriers as compared with the advanced tumor model for common antitumor activity experiments.

Combretastatin A-4 is known as an anticancer drug that acts to tubulin by disrupting tumor vessels (8–18). One of the combretastatin A4 derivatives, Cderiv, was developed by Hatanaka *et al.* and Ohsumi *et al.* in 1998 (Fig. 1a) (10,11). Cderiv also exhibited a powerful vascular disrupting effect by intraveneous injection (8–10). The vascular disrupting effect is induced by strong interruption of tumor blood flow, which prevents nutrient supply to solid tumors and leads to necrosis in tumors (15–18). Recently, our research showed that Cderiv changed microenvironments of microtumors so that the new environments were similar to the environments characteristic of advanced tumors (19). Namely, the treatment of Cderiv induced the EPR effect in 1 mm of microtumors. A detailed whole mechanism of combretastatin A-4 derivatives including Cderiv is not completely understood yet; however, morphological and functional alternations have been seen in endothelial cells (15). Most likely, Cderiv acts indirectly in contractile arterioles of tumors, rather than directly on tumor vessels. This Cderiv pretreatment would be a new methodology to enhance EPR-effect-based delivery of therapeutic agents, as well as diagnostic agents.

Evaluation of pharmacokinetics, biodistribution, and especially drug delivery efficiency by non-invasive imaging techniques has recently become more important (20–22). Of several modalities, such as PET, CT, and MRI, MRI is a non-invasive method for three-dimensional images with high spatial resolution. Paramagnetic gadolinium chelates, such as gadolinium(III) chelates, are often used as MRI contrast agents to enhance the signal in target tissues where the contrast agents are localized (23).

A previous report on a polymeric micelle MRI contrast agent showed passive accumulation in a solid tumor, resulting in intensive enhancement of T_1-weighted signals in the tumor tissues (24). This MRI contrast agent exhibited similar pharmacokinetics as compared to a polymeric micelle anticancer drug carrier, adriamycin-encapsulating polymeric micelle (ADR-micelle) (25,26). Their structures are shown in Fig. 1b and c. As well as the pharmacokinetics, biodistribution including tumor accumulation of the MRI contrast agent was similar to that of the ADR-micelle. For example, 24.6% and 22.5% of injected dose of the ADR-micelle and the polymeric micelle MRI contrast agent were found in blood at 24 h after intravenous injection, respectively. Accumulations in C26 tumor tissues were 9.6%ID/g and 6.1%ID/g at 24 h for the ADR-micelle and the contrast agent, respectively. These results indicated that the tumor diagnosis by means of the polymeric micelle MRI contrast agent can help to predict the targeting efficiency

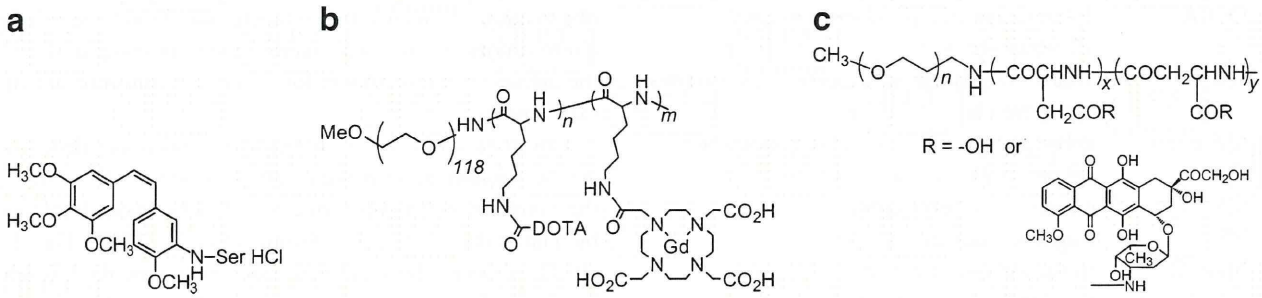

Fig. 1 Structure of (**a**) Cderiv, (**b**) polymeric micelle MRI contrast agent, and (**c**) ADR-micelle.

of the anticancer-drug-encapsulating polymeric micelle, such as the ADR-micelle.

The combination of a therapeutic drug and a diagnostic contrast agent incorporated in the same carrier system can be considered effective in the evaluation of therapeutic efficacy. This system would be a great potential for improvement of therapeutic efficacy, called as "theragnosis."

Cderiv was used to enhance permeability for improvement of the tumor targeting efficiency of a polymeric micelle carrier system. We evaluate in the present study whether Cderiv pretreatment enhances the tumor targeting of the polymeric micelle MRI contrast agent and the adriamycin-encapsulated polymeric micelle. The current study performed an MRI to evaluate the signal intensities in the tumor area. Antitumor activity was studied when this combination of the Cderiv pretreatment with ADR-micelles was used on 44As3-bearing mice (27).

MATERIALS AND METHODS

Preparation of Polymeric Micelle MRI Contrast Agents

Preparation of a polymeric micelle MRI contrast agent was reported previously (24). Briefly, a polymerization of Lys(Z) *N*-carboxy anhydride from PEG-NH_2 (Mw = 5,200) gave a poly(ethylene glycol)-b-poly[ε-(benzyloxycarbonyl)-L-lysine] (PEG-P(Lys(Z)). PEG-P(Lys(Z)) was dissolved in trifluoroacetic acid. Anisole and methanesulfonic acid were added to the solution. The mixture was stirred for 1 h to hydrolyze the protecting group. The solution was diluted with distilled water, then the excess of acid was extracted with diethylether until an organic layer became neutral. The obtained aqueous layer was neutralized by an addition of triethylamine, and dialyzed against 0.02 N NaOH and distilled water against SpectraPor 6 (MWCO = 1 k) membrane. Lyophilization gave white powder of PEG-P(Lys).

The obtained a poly(ethylene glycol)-b-poly(L-lysine) (PEG-P(Lys)) was a fully conjugated using mono *N*-hydroxysuccinimide ester of 1,4,7,10-Tetraazacyclododecane- 1,4,7,10-tetraacetic acid (DOTA) (1.3 eq *vs* lysine residues) and triethylamine in dried DMF. The reaction mixture was stirred overnight at 50°C. The resulting mixture was first dialyzed against 0.02 N HCl and then against distilled H_2O 5 times. The obtained polymer was dissolved in H_2O at a polymer concentration higher than 15 mg/mL and dialyzed against H_2O 3 times. Lyophilization gave poly(ethylene glycol)-*b*-poly(L-lysine-DOTA) (PEG-P(Lys-DOTA)) as white powder.

The conjugation was confirmed by ^{1}H-NMR under an alkali condition (pH > 10 in D_2O). The conjugated number of DOTA moiety was calculated from peak ratio between CH_2 protons of PEG at 3.73 ppm and 26H of DOTA and lysine protons in the range between 3.36 and 2.18 ppm.

The DOTA-conjugated block copolymer, PEG-P(Lys-DOTA), was mixed with $GdCl_3 \cdot 6H_2O$ at 50°C for 3 h in the range of pH 6–6.5. After several dialyses against water, Gadolinium-chelated PEG-P(Lys-DOTA-Gd) was obtained. ICP (SPS7800, SII Nano Technology Inc., Tokyo, Japan) was used for the determination of gadolinium content in the polymer. This block copolymer formed a polymeric micelle in an aqueous solution, and we detected the formation of polymeric micelle by DLS and GPC analysis.

Preparation of Adriamycin-Encapsulated Polymeric Micelles (ADR-micelles)

An adriamycin (ADR)-encapsulated polymeric micelle (ADR-micelle) was prepared according to a previously reported procedure (24,25). First, a block copolymer, poly (ethylene glycol)-*b*-poly(aspartic acid) (PEG-P(Asp)) (PEG_{Mw} = 12,000, Asp unit = 19), was synthesized from poly(ethylene glycol)-*b*-poly(β-benzyl L-aspartate). ADR was chemically conjugated to the aspartic acid of the block copolymer by EDC-mediated coupling reaction (63% conjugation to Asp unit). Then, free ADR was physically encapsulated in the block copolymer, which formed a polymeric micelle. ADR·HCl was dissolved in DMF with 1.3 equivalents of triethylemiane (*vs* ADR·HCl), and the ADR solution was mixed with the chemically ADR-

conjugated PEG-P(Asp-ADR). The mixture was stirred for 2 h at room temperature. The mixture was dialyzed with SpectraPor6 membrane against distilled water. The obtained solution was concentrated by polyethersulfone ultrafiltration membrane (MWCO = 100 k) equipped with an ultrafiltration unit (Amicon, Stirred Ultra Filter Cell). Physically encapsulated ADR was determined by an HPLC system (LC-2000 series, Jasco, Tokyo, Japan) equipped with a μBondasphere (Waters, Tokyo, Japan) column in acetonitrile/H_2O (including 1% of acetic acid) as an eluent. ADR was detected by measuring the absorbance at 485 nm. The conjugated ADR was worked only for stable encapsulation of free ADR, and no release of free ADR from the conjugate was found (28). We discussed only the physically encapsulated ADR for the determination.

MRI Study of Colon 26 CDF_1 Mice

Isoflurane (1.0–1.5%) was used for anesthesia in the MRI study. CDF_1 female mice bearing a colon 26 tumor ($n=4$) were intravenously injected with Cderiv (Tokyo Kasei Kogyo Co.) at a dose of 20 mg/kg. The size of the tumors was 50–150 mm^3. Either 72 h or 24 h from the Cderiv pretreatment, polymeric micelle MRI contrast agent was injected at a dose of 0.05 mmol Gd/kg into a mice tail vein.

MR images were taken with a Varian NMR system at 9.4T magnetic field. We performed a T_2-weighted fast spin echo (TR = 2,500 ms, ETL = 8, ESP = 4, effective TE = 48) and a T_1-weighted gradient echo (TR/TE = 8.0/4.2, flip angle = 30°, field of view of 50 × 30 mm, a matrix size of 192 × 192, and 2 mm for coronal thickness, and TR/TE = 8.0/4.5, flip angle = 30°, field of view of 45 × 45 mm, a matrix size of 192 × 192, and 2 mm for axial thickness). The signal intensity of the ROI was compared with the intensity of a stock solution of 0.1 mM gadolinium ion in agarose gel. For quantitative determination of gadolinium content in colon 26 tumor, the tumor samples were dissolved in the acid mixture of 98% H_2SO_4 and 62% HNO_3, and oxoammonium salt (1:2:1, v:v:v), and then were determined by means of ICP. For normalized signal intensity relative to the T_1-weighted images, the tumor area was selected as a ROI. The signal intensity of the ROI was compared with the intensity of a stock solution of 0.1 mM gadolinium ion in agarose gel. The relative signal intensity of the ROI at 24 h after the MRI contrast agent injection was compared to the signal intensity before the injection.

In Vivo Antitumor Activity

Antitumor activity against solid tumors was evaluated in human gastric scirrhous carcinoma 44As3-bearing nude mice. Tumor cells (44As3, 5.0×10^5) were transplanted into BLAB/C female nude mice ($n=6$) subcutaneously. BALB/c female nude mice bearing the 44As3 tumor were intravenously injected with Cderiv at a dose of 20 mg/kg at 10 days after the transplantation of 44As3 cells. ADR-micelles were injected at a dose of 10 mg/kg of physically entrapped ADR at 24 h after the Cderiv pretreatment. The mice in all cases were survived after the experiments finished at day 25. The tumor volumes and the body weights were measured at defined time intervals until 25 days after the drug treatments. The tumor volumes were calculated as follows: volume = $1/2LW^2$, where L is the long diameter and W is the short diameter of a tumor.

Animals

Five-week-old CDF_1 female mice were purchased from the Sankyo Labo Service Corporation, Tokyo, Japan. Six-week-old BALB/c female mice were purchased from CLEA Japan, Inc. All animal experiments were carried out in accordance with the guidelines of the Guiding Principles for the Care and Use of Laboratory Animals.

RESULTS AND DISCUSSION

Synthesis

Our polymeric micelle MRI contrast agent was used to observe the effect of Cderiv on tumor targeting. The Gd-DOTA-conjugated poly(ethylene glycol)-b-poly(L-lysine) block copolymer (PEG-P(Lys-DOTA-Gd)) formed a polymeric micelle as detected by means of DLS and GPC. This stably formed polymeric micelle exhibited both the characteristic long circulation in the blood and enough tumor accumulation to obtain MRI signals in the tumor tissue of colon 26-bearing mice, as reported previously (24). The blood half-lives of the polymeric micelle MRI contrast agent were 6.7 h and 18.4 h for α- and β-phases, respectively. This polymeric micelle MRI contrast agent exhibited pharmacokinetics behavior similar to that of an adriamycin-encapsulated polymeric micelle (ADR-micelle) (25,26). The advantage of this MRI contrast agent for the present work is that the MRI contrast agent informs us of the position and the amount of such a polymeric micelle MRI contrast agent in the tumor tissues, namely prediction of the drug targeting efficacy of ADR-micelle can be obtained.

Accumulation of Polymeric Micelles into Colon 26-Bearing Mice

Dose dependencies of Cderiv on tumor blood flow were evaluated previously (12). Intravenous injection of 1 and 3 mg/kg of Cderiv increased mean arterial blood pressure

for 2–3 h. The tumor blood flow was significantly decreased and was recovered in 2–4 h. However, the increased blood pressure at the dose of 10 mg/kg of Cderiv was maintained for 4–5 h, and the tumor blood flow was completely shut off among 8 h experiment. More than dose at 10 mg/kg of Cderiv caused long lasting tumor blood flow stasis for targeting of anticancer drug or diagnostic agent. Cderiv was intravenously injected at a dose of 20 mg/kg. The tumor blood flow stasis at this dose was reported to have continued for more than 6 h (13).

After the tumor blood flow stasis, some of the blood flows in the tumor vessels were recovered, and the others were not. Previous results showed that the Cderiv pretreatment remarkably enhanced permeability of the recovered and surviving tumor blood vessels (19). First, our polymeric micelle MRI contrast agent was injected at 72 h after Cderiv injection. The tumor tissues were taken out at 24 h after the contrast agent injection to determine gadolinium content in the tumor tissues by means of ICP measurement. As shown in Fig. 2a, significantly higher accumulation of the contrast agent was observed when Cderiv was pre-administered (9.8±0.8%ID/g for the Cderiv treatment (n=3) *vs* 5.6±1.0%ID/g tumor for the control (n=5), p value <0.001). This higher accumulation was due chiefly to the enhancement of the tumor vascular permeability induced by the Cderiv pretreatment, as observed in previous vital microscopic systems.

Then, time intervals of the Cderiv pretreatment were compared. When the polymeric micelle MRI contrast agent was injected at 24 h after the Cderiv pretreatment, 4.7±1.6%ID/g tumor tissues of the accumulation of the contrast agent were observed, as shown in Fig. 2b. However, when the contrast agent was injected at 72 h after the Cderiv injection, much higher accumulation in the tumor tissues was observed as described above (8.0± 2.5%ID/g tumor tissues). This lower accumulation of the contrast agent at 24 h was probably because of the ongoing blood flow stasis effect of Cderiv at this dose. Actually, the damage that the disrupting effect had on the tumor tissues was significant at 24 h after the Cderiv pretreatment in the case of the LY80 tumor model, and probably the contrast agent was not delivered effectively to tumor tissues because of poor tumor blood flow (19). However, at 72 h after the Cderiv pretreatment, the recovered tumor blood flow exhibited remarkable extravasation. This may explain why the polymeric micelle MRI contrast agent exhibited much higher accumulation in the tumor tissues at 72 h after the Cderiv pretreatment.

Enhancement of fluorescence intensities in the tumor tissues indicated the extravasation of FITC-labeled polymeric micelles from the tumor blood vessels (19); however, this fluorescence measurement was typically not quantitative analysis. Previous report used FITC-labeled polymeric micelles to observe the extravasation into tumor tissues. The polymeric micelle formed from FITC-labeled poly (ethylene glycol)-b-poly(b-benzyl L-aspartate) (PEG-PBLA-FITC, molecular weight, 15,300; Mw of PEG chain, 12,000; number of BLA units, 14.0). The size of FITC-labeled polymeric micelles exhibited 48.2±8.8 nm (the weight-average diameter ± SD). Enhancement of fluorescence intensities at both 24 h and 72 h after the pretreatment in the tumor tissues indicated the extravasation of FITC-labeled polymeric micelles from the tumor blood vessels (19); however, this fluorescence study was not of as quantitative measurements as measurements by means of ICP. Both cases exhibited the extravasation of FITC-labeled polymeric micelles; however, MRI as well as ICP measurement gave a quantitative amount of the polymeric micelle MRI contrast agent in the tumor tissues. Even though such fluorescence data exhibited the extravasation of polymeric micelles from the tumor blood vessels both 24 h and 72 h after the Cderiv treatment, the exact amount of the extravasated polymeric micelles in the tumor tissues was not measured. In contrast, the amount of the MRI contrast agent in tumor tissues at 72 h after the Cderiv pretreatment was quantitatively obtained through measurements of gadolinium amounts by means of ICP. A larger accumulation of 72 h post the Cderiv pretreatment was found than that of at 24 h, as shown in Fig. 2b. However, the nature of the tumor blood vessels' permeability by means of the Cderiv pretreatment remains unclear; it is thought to depend on tumor type and size. In colon 26 case, an accumulation of the polymeric micelle MRI contrast agent significantly enhanced at 72 h after the Cderiv pretreatment.

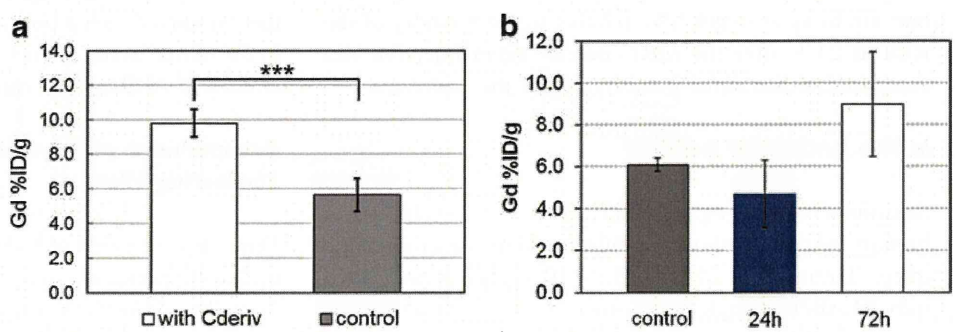

Fig. 2 Time interval effect of the Cderiv pretreatment on an accumulation of the polymeric micelle MRI contrast agent in colon 26 tumor tissues. (**a**) Either the Cderiv pretreatment at 72 h before the contrast agent injection (n=3) or without the treatment (n=5). (**b**) Control (n=3), the pretreatment at 24 h (n=4), and at 72 h (n=4), respectively. *** indicates P-value <0.001 (student's t-test).

MRI Study of Cderiv Pretreated Mice

Administration of Cderiv affected tumor vascular permeability, as we previously reported (19). An MRI study of the time interval study as shown in Fig. 2a was performed to observe accumulation of our polymeric micelle MRI contrast agent with the Cderiv pretreatment. When this contrast agent was used for tumor imaging in colon 26-bearing mice, a significant signal enhancement on the tumor T_1-weighted image was observed at 24 h (24). As described above section "Accumulation of Polymeric Micelles into Colon 26-Bearing Mice," in Fig. 2a, the significant difference of the accumulation of the contrast agent was found when Cderiv was pretreated at 72 h before the contrast agent injection. Figure 3 shows the axial T_1-weighted image of the tumor region (yellow circle) (a) with Cderiv treatment and (b) without treatment. A more than 2-fold (2.2 times) signal enhancement in the tumor region was observed at 24 h after the contrast agent injection (Fig. 3a). Without Cderiv treatment, 1.6 times of the signal enhancement was observed at 24 h after the injection compare to the before injection.

As well as the axial T_1-weighted image, the coronal slices exhibited characteristic images in the tumor tissues. Relatively high signal intensities were observed in the tumor-specific region, as shown in Fig. 4a (arrows). As compared to the coronal T_1-weighted images (Fig. 4a), the coronal T_2-weighted images also exhibited a curved-shape high-contrast region in the tumor tissues (Fig. 4b arrows). This relatively high contrast in the T_2-weighted image was observed before the injection of the contrast agent. Most likely, this region was caused by the Cderiv pretreatment resulting in a vasogenic edema formation. The whole mechanism of combretastatins including Cderiv on tumor vascularity is not still clear. However, evidence to date indicated the mechanism of combretastatins treatment. Combretastatins affected both morphological and functional changes in endothelial cells after the injection (9,17). Combretastatins act to the endothelial cell after the injection, which involves the damage and shape change of endothelial cells (15,16). The early effect after the combretastatin treatment on tumor vascularity was an increase in the permeability to macromolecules. This increase in the permeability leads to forming edema in tissues, and this could be increased in interstitial fluid pressure. Decreasing blood fluidity and stacking red blood cells were found in blood vessels. These events lead to vasoconstriction of the tumor vascularity.

Our previous report describes that surviving or restored tumor blood vessels exhibited a remarkable enhancement of permeability of FITC-labeled polymeric micelles after the Cderiv pretreatment (19). Figure 4c shows a merged image of the coronal T_1- or T_2-weighted tumor at the same position. The high-contrast region in the T_1-weighted image (arrow) was positioned adjacent to the T_2-weighted high-contrast region (arrow heads). These results support the assertion that the extravasation of the tumor blood vessels around such a T_2-high-contrast region was remarkably

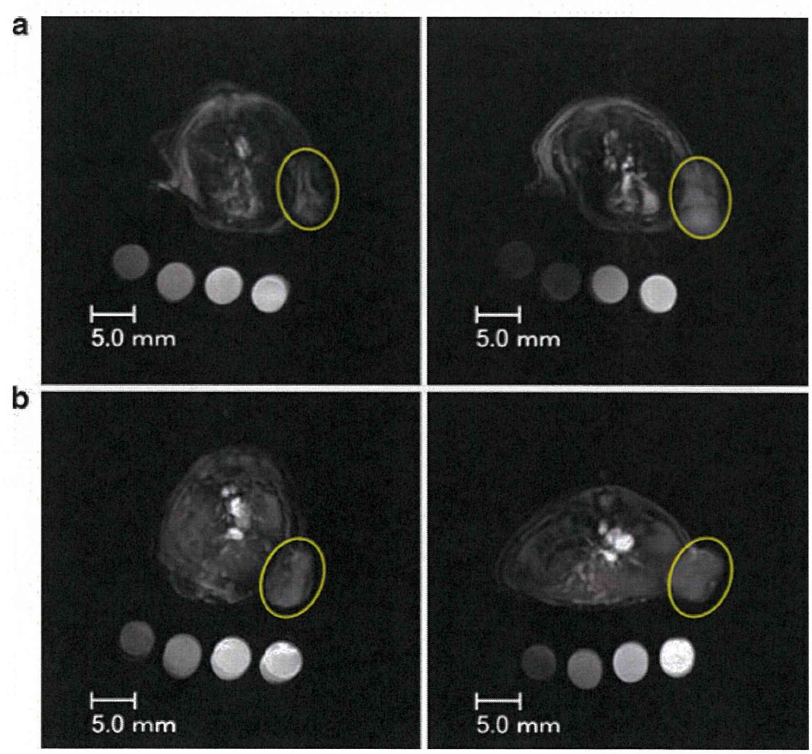

Fig. 3 Axial slices of the T_1-weighted MIP image of (**a**) Cderiv treatment at 72 h before the contrast agent injection (*left*) before and (*right*) 24 h, (**b**) without treatment (*left*) before and (*right*) 24 h.

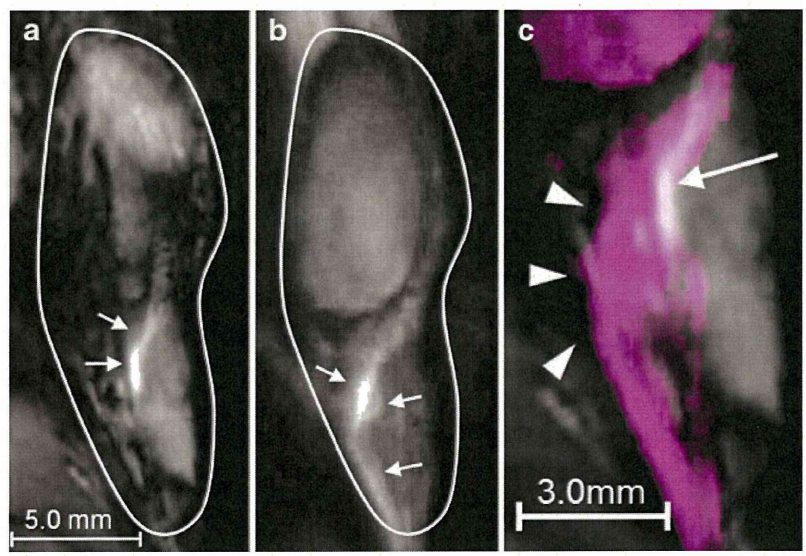

Fig. 4 Coronal slices of tumor area of (**a**) the T_1-weighted image and (**b**) the T_2-weighted image at 24 h after the injection. (**c**) A merged image of the T_1-weighted scenario (*gray*) and the T_2-weighted scenario (*magenta*) of the expanded tumor area. *Arrows* and *arrow heads* indicate the intense region of the T_1-weighted and the T_2-weighted images, respectively.

enhanced. One related result was a higher concentration of the polymeric micelle MRI contrast agent in the tumor tissues. So far, there have been no reports of an accumulation of nanoparticles specific-regions in tumor by means of the EPR effect. In terms of tumor diagnosis, high concentrations of the MRI contrast agent in such a part of the region led to the intense signal compared with the case of homogeneous distribution in a whole region of the tumor tissues. In this report, a higher accumulation of the MRI contrast agent in the tumor tissues was obtained by means of the Cderiv pretreatment. Furthermore, such a extravasated MRI contrast agent was locally concentrated in the specific region in which Cderiv might be worked. In general, the MRI contrast agent exhibits the T_1-shortening property of water protons. The concentration of the gadolinium ion significantly affected the T_1-shortening property, which would lead to the intense signal. Consequently, the observations in such specific contrast enhancement at the solid tumor help to distinguish the normal and the diseased tissues easily.

Anticancer drugs should be distributed through the whole region of the tumor tissues. Our previous report indicates that movements of macromolecules including polymeric micelles are strongly dependent on a perfusion of the tumor tissues. Namely, tumor-tissue perfusion can distribute a locally accumulated polymeric micelle encapsulating anticancer drug in the tumor tissues.

As we described in the introduction, the Cderiv pretreatment enhances the vascular permeability of the solid tumor even in microscopic tumors. In recent reports on tumor permeability for a drug targeting system, a tumor environment change by a TGF-β receptor inhibitor (TβRI) emerged for the EPR effect enhancement. TβRI induced alternation of tumor neovasculature that lead to enhanced permeability of nanoparticles (29,30). However, function of TGF-β inhibitor is diverse, and the use of such a TGF-β inhibitor for tumor permeability must carefully address the dose and side effect. On the other hand, nitroglycerin, classical medication for angina topically or orally, was examined for the EPR effect

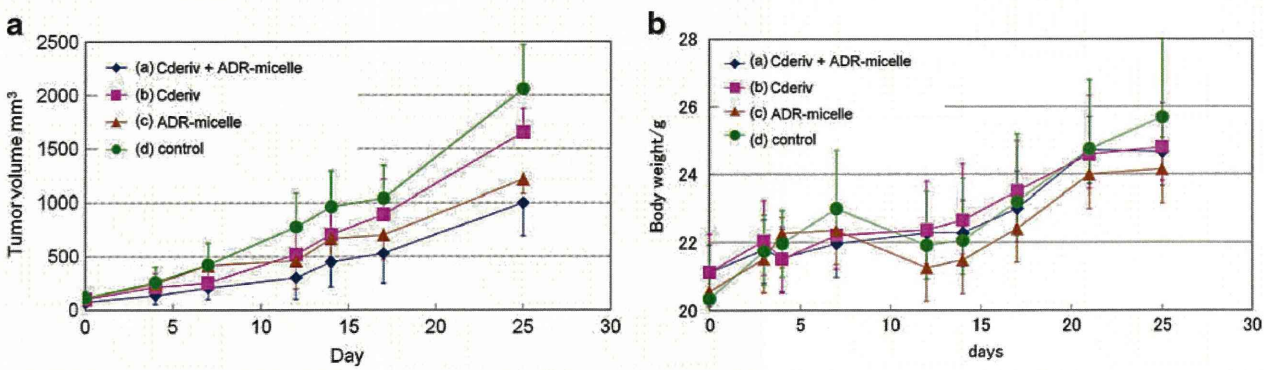

Fig. 5 (**a**) Antitumor activity of 44As3-bearing mice ($n = 6$) and (**b**) the body weight change after a single injection of (a) Cderiv + ADR-micelle, (b) Cderiv, (c) ADR-micelle, and (d) control.

enhancement. Topical application of nitroglycerin that converts to nitric oxide enhanced tumor permeability for targeting of macromolecular antitumor drugs (31,32). In contrast, Cderiv acts as a vascular disrupting agent at the tumor-specific blood capillaries. An anticancer drug targeting system supported with the Cderiv pretreatment can overcome a problem with the delivery of the nanocarriers. Because the delivery of anticancer drugs would strongly depend on the tumor vascular system, the tumor blood vessels would need to be opened to extravasate the nanocarriers. This combination greatly enhanced their permeability, resulting in the high accumulation in the solid tumor. Also, when locally accumulated, the contrast agent exhibited a relatively high signal-to-noise (S/N) ratio. This was the case of the MRI contrast agent; however, a polymeric micelle encapsulating anticancer drug could accumulate with the Cderiv pretreatment.

Antitumor Activity Relates to the Cderiv Pretreatment with ADR-Micelles Targeting 44As3 Human Gastric Scirrhous Carcinoma-Bearing Mice

Diagnosis of this scirrhous gastric carcinoma is quite difficult because of pathological features of this gastric cancer in humans. Highly progressed peritoneal dissemination or distant metastasis to lymph nodes has been observed in many cases. Due to a problem of anticancer drug targeting into this gastric cancer, this gastric scirrhous carcinoma usually generates a poor prognosis even after resection in humans. Targeting of anticancer drug into such tumor model has been highly desired (33). Antitumor activity of a single injection of ADR-micelle with the Cderiv pretreatment in 44As3 human gastric scirrhous carcinoma was evaluated by monitoring of tumor growth, as shown in Fig. 5. The dose of Cderiv and the dose of ADR-micelles were 20 mg/kg and 10 mg/kg, respectively.

Cderiv itself exhibited antitumor activity by disrupting tumor blood vessels. ADR-micelles exhibited better antitumor activity than the Cderiv treatment alone. To observe the antitumor activity, the current study used a combination of the Cderiv pretreatment with ADR-micelles. There was no statistically significant difference between the combination of Cderiv with ADR-micelles and ADR-micelles; however, this result indicates that the combination was effective for suppressing tumor growth.

In this animal experiment, we injected 10 mg/kg of ADR-micelles at 24 h after the Cderiv pretreatment. We observed enhancement of tumor permeability in LY80 tumors when Cderiv was administered at 24 h before the FITC-micelle injection (19). However, from the biodistribution study of the polymeric micelle MRI contrast agent, the contrast agent accumulated much higher concentration in the tumor tissues when Cderiv was pretreated at 72 h before the injection. In this 44As3 case, the tumor blood flow may not be recovered at 24 h after the Cderiv treatment. The effects of Cderiv on each tumor models were not known in the appropriate time to pre-treat before ADR-micelle injection.

So far, this experiment did not show serious side effects with a multiplier anticancer drug combination. In terms of the body-weight change, no difference was observed to compare with the control and the others, as shown in Fig. 5b. This combination might have an optimum time interval and dose for the antitumor activity. Also, detailed movements of the polymeric micelles after local accumulation in the tumor tissues are not yet clear; however, this combination may have a chance to be a new concept underlying nanocarrier-based antitumor drug targeting systems.

CONCLUSION

A vascular disrupting agent, Cderiv, enhanced the tumor accumulation of a polymeric micelle MRI contrast agent in the tumor tissues. An MRI shows that the signal intensities of the T_1-weighted images of the tumor area greatly enhanced at 24 h after the MRI contrast agent injection. The MRI study indicates that there was observable local accumulation of the polymeric micelles in the tumor-specific region which led to relatively high signal intensity in the tumor tissues. This T_1-relatively high region was positioned adjacent to the T_2-weighted high-contrast region. The pretreatment of Cderiv changed the tumor environment, leading to extravasation of the polymeric micelles in the tumor tissues. The combination of the Cderiv pretreatment and ADR-micelles exhibited better tumor-growth suppression of 44As3 human gastric scirrhous carcinoma. The Cderiv pretreatment enhanced tumor accumulation of the polymeric micelle MRI contrast agent. We expect a combination therapy of a polymeric micelle anti cancer drug with the Cderiv pretreatment can exhibit greater antitumor activity than a single agent's therapy through optimization in doses of both agents as well as in the interval between the two agents' injections.

REFERENCES

1. Matsumura Y, Maeda H. A new concept for macromolecular therapeutics in cancer chemotherapy: mechanism of tumoritropic accumulation of proteins and the antitumor agent Smancs. Cancer Res. 1986;46:6387–92.
2. Aliabadi HM, Lavasanifar A. Polymeric micelles for drug delivery. Expert Opin Drug Deliv. 2006;3(1):130–62.

3. Torchilin V. Tumor delivery of macromolecular drugs based on the EPR effect. Adv Drug Deliv Rev. 2011;63:131–5.
4. Amantea MA, Forrest A, Northfelt DW, Nanelok R. Population pharmacokinetics and pharmacodynamics of pegylated-liposomal doxorubicin in patients with AIDS-related Kaposi's sarcoma. Clin Pharmcol Ther. 1997;61:301–11.
5. Duncan R. Polymer conjugates as anticancer nanomedicines. Nat Rev Cancer. 2006;6:688–701.
6. Duncan R. The dawning era of polymer therapeutics. Nat Rev Drug Discov. 2003;2:347–60.
7. Hori K, Nishihara M, Yokoyama M. Vital microscopic analysis of polymeric micelle extravasation from tumor vessels: macromolecular delivery according to tumor vascular growth stage. J Pharm Sci. 2009;99(1):549–62.
8. Pettit GR, Singh SB, Hamel E, Lin CM, Alberts DS, Garcia-Kendall D. Isolation and structure of the strong cell growth and tubulin inhibitor combretastatin A-4. Experientia. 1989;45(2):209–11.
9. Tozer GM, Kanthou C, Parkins CS, Hill SA. The biology of the combretastatins as tumour vascular targeting agents. Int J Exp Pathol. 2002;83(1):21–38.
10. Hatanaka T, Fujita K, Ohsumi K, Nakagawa R, Fukuda Y, Nihei Y, *et al.* Novel B-ring modified combretastatin analogues: syntheses and antineoplastic activity. Bioorg Med Chem Lett. 1998;8(23):3371–4.
11. Ohsumi K, Nakagawa R, Fukuda Y, Hatanaka T, Morinaga Y, Nihei Y, *et al.* Novel combretastatin analogues effective against murine solid tumors: design and structureactivity relationships. J Med Chem. 1998;41(16):3022–32.
12. Hori K, Saito S, Nihei Y, Suzuki M, Sato Y. Antitumor effects due to irreversible stoppage of tumor tissue blood flow: evaluation of a novel combretastatin A-4 derivative, AC7700. Jpn J Cancer Res. 1999;90 (9):1026–38.
13. Hori K, Saito S. Microvascular mechanisms by which the combretastatin A-4 derivative AC7700 (AVE8062) induces tumour blood flow stasis. British J Cancer. 2003;89:1334–44.
14. Hori K. Cancer therapy by means of irreversible tumor blood flow stasis: Starvation tactics against solid tumors. Gene Ther Mol Biol. 2005;9:203–16.
15. Tozer GM, Kanthou C, Baguley BC. Disrupting tumour blood vessels. Nat Rev Cancer. 2005;5:423–35.
16. Griggs J, Metcalfe JC, Hesketh R. Targeting tumour vasculature: the development of combretastatin A4. Lancet Oncol. 2001;2(2):82–7.
17. Tozer GM, Prose VE, Wilson J, Cemazar M, Shan S, Dewhirst ME, *et al.* Mechanism associated with tumor vascular shut-down induced by combretastatin A-4 phosphate: intravital microscopy and measurement of vascular permeability. Cancer Res. 2001;61:6413–22.
18. Kim TJ, Ravoori M, Landen CN, Kamat AA, Han LY, Lu C, *et al.* Antitumor and antivascular effects of AVE8062 in ovarian carcinoma. Cancer Res. 2007;67(19):9337–45.
19. Hori K, Nishihara M, Shiraishi K, Yokoyama M. The combretastatin derivative (Cderiv), a vascular disrupting agent, enables polymeric nanomicelles to accumulate in microtumors. J Pharm Sci. 2010;99(6):2914–25.
20. Veiseh O, Gunn JW, Zhang M. Design and fabrication of magnetic nanoparticles for targeted drug delivery and imaging. Adv Drug Deliv Rev. 2010;62(3):284–304.
21. Sun C, Lee JSH, Zhang M. Magnetic nanoparticles in MR imaging and drug delivery. Adv Drug Deliv Rev. 2008;60(11):1252–65.
22. Liu Y, Miyoshi H, Nakamura M. Nanomedicine for drug delivery and imaging: A promising avenue for cancer therapy and diagnosis using targeted functional nanoparticles. Int J Cancer. 2007;120(2):2527–37.
23. Caravan P, Ellison JJ, McMurry TJ, Lauffer RB. Gadolinium(III) chelates as MRI contrast agents: structure, dynamics, and applications. Chem Rev. 1999;99(9):2293–352.
24. Shiraishi K, Kawano K, Minowa T, Maitani Y, Yokoyama M. Preparation and *in vivo* imaging of PEG-poly(L-lysine)-based polymeric micelle MRI contrast agents. J Contr Release. 2009;136(1):14–20.
25. Yokoyama M, Okano T, Sakurai Y, Fukushima S, Okamoto K, Kataoka K. Selective delivery of adriamycin to a solid tumor using a polymeric micelle carrier system. J Drug Targeting. 1999;7(3):171–86.
26. Yokoyama M, Miyauchi M, Yamada N, Okano T, Sakurai Y, Kataoka K. Characterization and antitumor activity of the micelle-forming polymeric anticancer drug adriamycin-conjugated poly (ethylene glycol)-poly(aspartic acid) block copolymer. Cancer Res. 1999;50:1693–700.
27. Yanagihara K, Takigahira M, Tanaka H, Komatsu T, Fukumoto H, Koizumi F, *et al.* Development and biological analysis of peritoneal metastasis mouse models for human scirrhous stomach cancer. Cancer Sci. 2004;96(6):323–32.
28. Yokoyama M, Fukushima S, Uehara R, Okamoto K, Kataoka K, Sakurai Y, *et al.* Characterization of physical entrapment and chemical conjugation of adriamycin in polymeric micelles and their design for *in vivo* delivery to a solid tumor. J Contr Release. 1998;50(1–3):79–92.
29. Kano RM, Bae Y, Iwata C, Morishita Y, Yashiro M, Oka M, *et al.* Improvement of cancer-targeting therapy, using nanocarriers for intractable solid tumors by inhibition of TGF-β signaling. Proc Natl Acad Sci USA. 2007;104(9):3460–5.
30. Minowa T, Kawano K, Kuribayashi H, Shiraishi K, Sugino T, Hattori Y, *et al.* Increase in tumour permeability following TGF-β type I receptorinhibitor treatment observed by dynamic contrast-enhanced MRI. Br J Canc. 2009;101:1884–90.
31. Seki T, Fang J, Maeda H. Enhanced delivery of macromolecular antitumor drugs to tumors by nitroglycerin application. Cancer Sci. 2009;100(12):2426–30.
32. Maeda H. Tumor-selective delivery of macromolecular drugs via the EPR effect: background and future prospects. Bioconjugate Chem. 2010;21(5):797–802.
33. Nakajima TE, Yanagihara K, Takigahira M, Yasunaga M, Kato K, Hamaguchi M, *et al.* Antitumor Effect of SN-38–releasing polymeric micelles, NK012, on spontaneous peritoneal metastases from orthotopic gastric cancer in mice compared with irinotecan. Cancer Res. 2008;68(22):9318–22.

mRNA Delivery through Fibronectin Associated Liposome-Apatite Particles: A New Approach for Enhanced mRNA Transfection to Mammalian Cell

Fatema Tuj Zohra,[a,†] Yoshie Maitani,[b] and Toshihiro Akaike*,[a]

[a] *Department of Biomolecular Engineering, Graduate School of Bioscience and Biotechnology, Tokyo Institute of Technology; 4259 Nagatsuta-cho, Midori-ku, Yokohama 226–8501, Japan: and* [b] *Fine Drug Targeting Research Laboratory, Institute of Medicinal Chemistry, Hoshi University; 2–4–41 Ebara, Shinagawa-ku, Tokyo 142–8501, Japan.*
Received July 8, 2011; accepted October 13, 2011; published online October 26, 2011

It was believed for a long time that mRNA is very unstable, and can not be used for therapeutic purposes. In the last decade, however, many research groups proved its transfection feasibility along with advantages and applications. Our investigation is aimed at establishing a potent and efficient mRNA delivery system. We previously reported that an inorganic–organic hybrid carrier by exploiting the advantages of inorganic nano apatite particles onto organic carrier DOTAP {*N*-[1-(2,3-dioleoloxy)propyl]-*N*,*N*,*N*-trimethyl ammonium chloride} and showed potential effect of carbonate apatite particles on each of the mRNA delivery steps in dividing and non-dividing cell. Here, we report on the development of a more efficient mRNA carrier by complexing ECM protein, fibronectin with the DOTAP-apatite carrier. The carrier showed enhanced uptake of luciferase mRNA both qualitatively and quantitatively. Accelerated cellular endocytosis rate was evaluated using labeled endosome. Finally expression of lucifearse mRNA was higher for fibronectin complexed carrier in compared to the uncoated one.

Key words mRNA delivery; cationic lipid; carbonate apatite; fibronectin

mRNAis a relatively novel tool in gene delivery. This is due to the fact that it has been considered too labile to ensure protein expression. Numerous studies have demonstrated the contrary; not only is mRNA capable of tolerating the impact of transfection protocols and of being translated efficiently[1—7]; it also has some advantages over DNA. mRNA as a gene delivery tool is a very good alternative way to treat those cells where DNA based gene expression is little or very low due to the absence of cell cycle-dependent breakdown of the nuclear envelop.[8,9] The higher safety, due to the avoidance of genomic insertion, and no need to provide for a promoter and a terminator decide in favor of mRNA. Moreover mRNA is deprived of immunogenic CpG motifs, and hence displays reduced immunogenic effects.[10,11] When combined with the aforementioned advantages, this property makes it even more attractive to apply mRNA in the context of gene delivery. mRNA based expression of certain protein sustains for a limited time but such transient expression is desirable in some clinical disorders specially neurological disorders.[12,13] Vaccination with mRNA is definitely another broad area of application due to the superiority of mRNA compared to DNA or proteins in inducing an immune response as shown by many research groups.[14—19]

These studies imply mRNA-based gene delivery is growing huge interest for some pathological recovery and cancer vaccination and thus, further improvement of mRNA carrier is highly desirable.

Extracellular matrix (ECM) protein and adhesion molecules have been used for DNA based gene delivery. The arginin–glycine–aspartic acid (RGD) sequence is well known to serve as a recognition motif in multiple ligands for several different integrins such as integrin $\alpha v\beta 3$ and $\alpha 5\beta 1$ *etc.*[20] RGD-modified liposomes[21,22] and polymers[23,24] have been developed as gene transfer vectors. An electrostatic complex consisting of a cationic liposome, an integrin $\alpha 5\beta 1$-targeting peptide, and plasmid DNA, was efficiently transfected to tumor cells.[25,26] On the other hand, ECM proteins, especially collagen 1 and fibronectin which are intrinsically involved in development, homeostasis, and maintenance of bone or tooth, closely associate with deposited calcium phosphate (CaP) ceramics and thus act as scaffold for neighboring cells.[27—31] ECM molecules have the inherent tendency of binding to the charged surface of CaP derivatives by electrostatic interactions. Based on this natural phenomena, it has been reported that calcium phosphate/DNA complex with ECM proteins, especially collagen and fibronectin, led to remarkably high transgene expression in mammalian cells.[32]

We previously reported on a hybrid carrier by embedding inorganic nano-particles of carbonate apatite onto liposomal carrier *N*-[1-(2,3-dioleoloxy)propyl]-*N*,*N*,*N*-trimethyl ammonium chloride (DOTAP) and demonstrated its high transfection potency of Luciferase mRNA both in mitotic and non-mitotic cells.[3] We report here for the first time on the development of surface-functional composites of DOTAP-apatite with the help of fibronectin and succeed in enabling rapid cellular endocytosis and high luciferase-mRNA delivery in cytoplasm and eventual enhancement in transgene expression.

MATERIALS AND METHODS

Cell Culture HeLa cell lines were cultured in 25-cm^2 flasks in Dulbecco's modified Eagle's medium (DMEM) supplemented with 10% fetal bovine serum (FBS), 50 μg penicillin/mL, 50 μg streptomycin/mL and 100 g neomycin/mL at 37°C in a humidified 5% CO_2 containing atmosphere.

Synthesis of mRNA Transcripts mRNA encoding luciferase was prepared by *in vitro* transcription of the luciferase SP6 control DNA having a poly(A) tail [A30] (Promega,

† Present address: *Fine Drug Targeting Research Laboratory, Institute of Medicinal Chemistry, Hoshi University; 2–4–41 Ebara, Shinagawa-ku, Tokyo 142–8501, Japan.*

* To whom correspondence should be addressed. e-mail: takaike@bio.titech.ac.jp

U.S.A.) using an SP6 RiboMAX™ kit as described by the manufacturer (Promega) with or without m7G(5′)pppG(5′) cap analog (Ambion, U.S.A.) at a ratio of 5:1 cap/guanosine 5′-triphosphate (GTP). When the cap analog was omitted, the GTP concentration was raised accordingly to 5 mM. *In vitro* transcribed mRNAs (with or without cap) were characterized by gel electrophoresis and were all *ca.* 1800 bp in length. Purification of mRNA was performed by RQ1 DNase I digestion, followed by extraction with phenol:chloroform:isoamyl alcohol and precipitation by addition of sodium acetate (pH 5.5) and ethanol. Precipitated RNA was washed with 70% ethanol, dissolved in water, quantified spectrophotometrically at 260 nm and examined by agarose gel electrophoresis after denaturation at 65°C for 15 min.

Liposome Formation For the preparation of liposome, solid DOTAP, Sigma was initially dried from chloroform, subsequently dispersed in δH_2O and shaken at a temperature above the gel-to-liquid-crystalline transition temperature of the lipid (*ca.* 0°C) for 15 min, followed by sonication of the milky solution for 10 min.

Complex Formation Three micrograms of heat-denatured mRNA (10 min at 65°C) and 6—10 μg of DOTAP were diluted separately in 100 μL DMEM media (pH 7.5). After 15 min, DOTAP was added to the RNA solution, followed by incubation for 15 min at room temperature. By adjusting final volume to 1 mL, 4 mM $CaCl_2$ and 0 to 50 μg/mL fibronectin solution were added prior to incubation for 30 min at 37°C. The solution containing each type of transfection complexes was added with 10% FBS to the rinsed cells. Treated cells were incubated at 37°C in a 5% CO_2 humidified environment for 2—4 h. After 4 h, the transfection mix was discarded and 1 mL of fresh serum medium was added to the cells. Cells were cultured for 6—12 h before analysis of reporter gene expression. The transfected cells were lysed by a lysis buffer (Promega) and the luciferase activity was measured using the luciferase assay system by a luminometer (TD-20/20 Luminometer, U.S.A.). Transfection efficiency was measured as mean light units per milligram of cell protein.

Labeling of mRNA mRNA has been labeled using fluorescein RNA labeling mix (Roche, Germany) which contains fliuorescein-12-uridine 5′-triphosphate (UTP) during *in vitro* transfection of luciferase control DNA according to the manufacturer's protocol. As recommended, the labeled probe was used immediately after the preparation.

Dynamic Light Scattering studies The size and zeta potential were measured by a light scattering apparatus, ELS 200TI (Otsuka Electronics, Osaka, Japan).

Flow Cytometry Fluorescein labeled mRNA containing complexes were added with 10% FBS to 80% confluent HeLa cells seeded in a 6-well plate and incubated for 3 h. Cells were lysed by trypsin–ethylenediaminetetraacetic acid (EDTA) and after detachment of the adherent cells centrifugation has been performed. Discarding supernatant the cell pallet was re suspended in 1 mL serum free DMEM media and used for EPICS XL flow cytometer (Beckman Coulter, CA, U.S.A.). The intensity of fluorescein labeled mRNA in HeLa cell was determined by gating cells at an excitation wavelength of 488 nm using an argon ion laser. The presence of the labeled mRNA was detected by emission at a wavelength of 525 nm.

Confocal Microscopy The cells were grown on presterilized coverslips inside a petridish filled with the appropriate culture medium and after reaching the desired confluency the cell were transfected with fluorescein-labeled mRNA. After certain periods (1 to 5 h), acidic compartments like endosomes were labeled with Lysotracker red DND-99 (diluted to 50—75 nM in phosphate buffered saline (PBS)). For labeling, the medium containing transfection mix were removed and the pre-warmed (37°C) probe containing medium was added and incubated for 30 min at 37°C. After removing the probe solution, fresh serum-free DMEM was added and incubated again at 37°C for distaining. After fixing the labeled cell using formalin they were observed under FLUOVIEW confocal laser scanning microscope (OLYMPUS).

RESULTS AND DISCUSSION

Determination of Size and Surface Charge of the Particles After the formation of mRNA-DOTAP-apatite complex with or without fibronectin, the initial characterization has been performed. It was found that particle size was gradually decreased from 660 to 361 nm after the complexation of mRNA-DOTAP-apatite particles with different concentrations of fibronectin (Fig. 1). We can speculate that the presence of fibronectin protects non-specific interaction with other serum proteins and also prevent aggregation of liposome particles. Zeta potential also decreased from +18 to −10 mV due to the complexation of fibronectin with the mRNA-DOTAP-aptite particles. This strategy of significant change in size and charge clearly suggested fibronectin coating on mRNA-DOTAP-apatite particles. It is well known that an optimum positive charge of gene-carrier complex is the pre-requisite to bind on the cell membrane for subsequent uptake. In this regards, even though, after addition of fibronectin, the surface charge of the particles is decreased from positive to entirely negative, enhanced binding and internalization is expected due to cell surface integrin mediated uptake mechanism.

Analysis of Uptake of the Labeled Luc-mRNA In order to demonstrate whether DOTAP-apatite particles functionalized with fibronectin can facilitate enhanced delivery of labeled mRNA across the plasma membrane, we examined cellular uptake of the fluorescein labeled mRNA, following 3 h incubation of HeLa cells with various particle formulations. As shown in Fig. 2, while with only DOTAP, delivery of

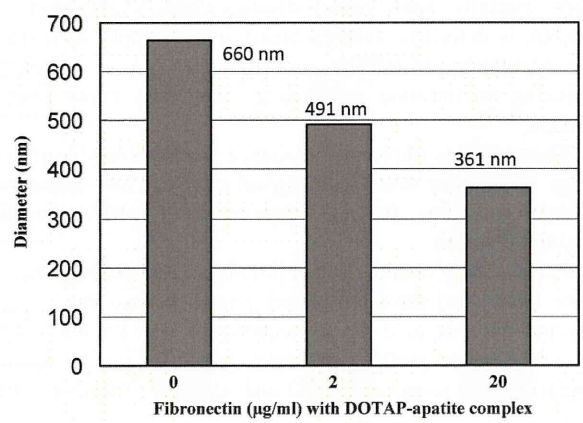

Fig. 1. Size of the Particles

DOTAP-apatite complexes with or without fibronectin (2—20 μg/mL) were prepared as described in the method section. Average size of three particles is presented here.

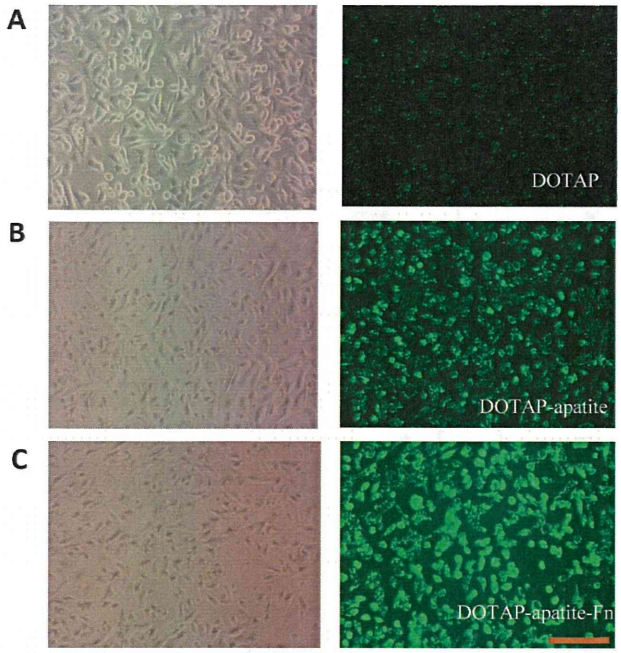

Fig. 2. Cellular Uptake Analysis of Fluorescein Labeled mRNA into HeLa Cell by DOTAP-Apatite-Fn Particles

Fluorescein labeled mRNA-DOTAP, fibronectin coated or uncoated DOTAP-apatite complexes were prepared as described in the method section. Complexes were added with 10% FBS to 80% confluent HeLa cells seeded in a 24-well plate and incubated for 4 h. Extracellular particles were removed by EDTA prior to observation under a fluorescence microscope. Bar indicates 200 μm.

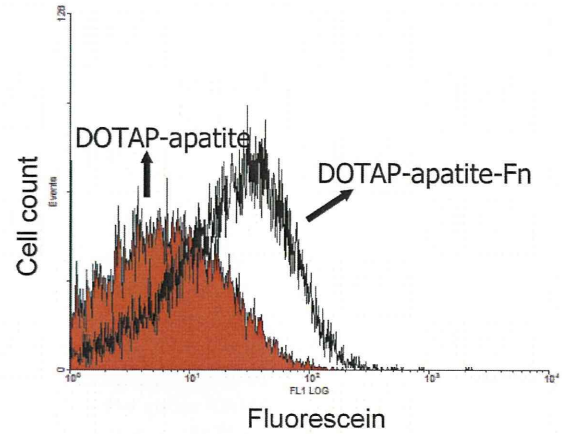

Fig. 3. Cellular Uptake Analysis by Flow Cytometry

Fibronectin coated or uncoated DOTAP-apatite complexes were prepared as described in the method section. Complexes were added with 10% FBS to 80% confluent HeLa cells seeded in a 6-well plate followed by incubation for 4 h. Cells were treated by trypsin-EDTA and after detachment of the adherent cells centrifugation have been performed. Discarding supernatant the cell pallet was resuspended in 1 mL serum free DMEM media and used for flow cytometry.

fluorescein labeled mRNA was very low (Fig. 2A), complexation of DOTAP with inorganic apatite resulted in significantly improved mRNA delivery (Fig. 2B). Moreover, when DOTAP-apatite paricles were complexed with fibronectin and allowed to deliver particle bound mRNA, more pronounced cell associated labeled mRNA was observed (Fig. 2C). Quantitative analysis by flow cytometry also demonstrated the similar delivery potency by DOTAP-apatite-Fn particles compared to the particles without fibronectin (Fig. 3). This result indicates fibronectin facilitated enhanced mRNA uptake might be partly because of recognition by the extracellular domains of specific integrin molecules on the cell membrane.

For direct demonstration of endocytosis mediated internalization rather than fusion, different particles were allowed to deliver fluorescein labeled mRNA into HeLa cells (Fig. 4A) whose endosomes were stained with Lysotracker Red DND-99 probe (Fig. 4B) followed by incubation for 3 h. As shown in Fig. 4C (upper panel), higher numbers of fluorescein labeled mRNA were associated with endosome (as viewed

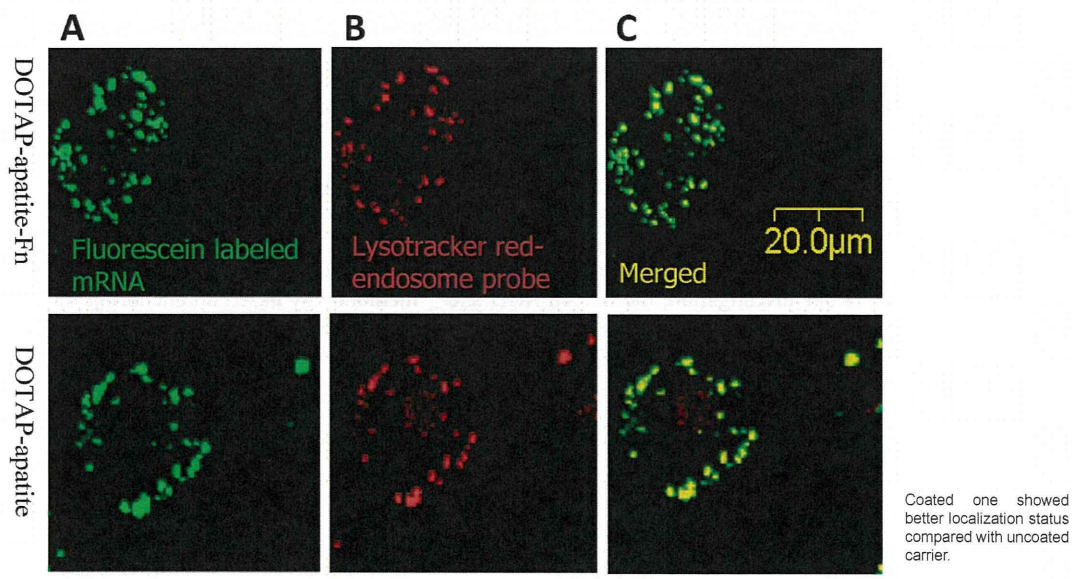

Fig. 4. Endosomal Localization of Labeled Luc-mRNA after 3 h

Fluorescein labeled mRNA was allowed to form fibronectin coated mRNA-DOTAP-apatite complex where 2 μg/mL of fibronectin was used. The complex was added with 10% FBS to 80% confluent HeLa cells seeded on cover slips inside a petridish. After 3 h, acidic compartments like endosomes/lysosomes were stained with Lysotracker red DND-99 (diluted to 50—75 nM in PBS) and incubated for 30 min. After replacing the labeling solution with fresh serum free medium, the cells were fixed and observed under confocal microscope. Green, red and yellow colors indicate on labeled mRNA (A), endosomes (B) and merged status (C) respectively. Bar indicates 20 μm.

from merged status) for fibronectin complexed DOTAP-apatite particles in comparision with the uncomplexed one (Fig. 4C, lower panel). This result, is again suggesting that the receptor mediated endocytosis might caused enhanced mRNA internalization through fibronectin complexed carrier and better level of co localized mRNA within a single cell in compared to the uncomplexed one.

Analysis of the Expression Pattern of Fibronectin Coated Particles We then examined the effect of fibronectin on the trasfection efficiency of DOTAP-apatite particles by checking the gene expression pattern in HeLa cell. As stated previously that optimum concentration of DOTAP was determined for a certain amount of luiciferase mRNA in HeLa cell by applying 4 to 16 μg of DOTAP along with 3 μg of Luc-mRNA to form either mRNA-DOTAP complex or mRNA-DOTAP-apatite complex.[5] Then mRNA-DOTAP-apatite-Fn complexes were formed using 2—50 μg/mL fibronectin and all the complexes were then allowed to transfect HeLa cells. Luciferase expression was determined at 6 h post transfection. The expression has been enhanced around 2 times due to the presence of fibronectin on the DOTAP-apatite particles as shown in Fig. 5A. Among the different concentrations, 2 μg/mL fibronectin showed maximum enhancement, then exhibited gradual decrease as concentration of fibronectin increases (Fig. 5A). Many parameters including size of delivery particles are known to influence transfection efficiency and larger particles are more efficient in transfection.[33,34] Thus this strategy of decreasing efficiency with increasing Fn concentration can be correlated with size of the particles. As size decreased for increasing fibronectin concentration, larger complexes with lower fibronectin value (2 μg/mL) exhibited maximum enhancement of the expression (Fig. 5A). On the other hand, even though bigger, DOTAP-apatite paricles had lower efficiency than the fibronectin complexed one due to better association with the cell. It is noteworthy that Fn-DOTAP-apatite particles showed more than 50 times enhanced transfection potency than the only DOTAP (the so far reported most efficient non-viral mRNA carrier). This result shows a potential way to significantly improve mRNA transfection potency over the existing liposome technology.

Fibronectin is a large (440 kDa) multidomain extracellular matrix protein with an RGD site that is not exposed in its native compact conformation. When complexed with liposome vector, fibronectin adopts a conformation that is more open than its compact conformation.[35] This open conformation exposes a hidden RGD site in Fn that stimulates binding to adhesion molecules. In our investigation, the hidden RGD site of the fibronectin coated complex might be exposed.

Proof of Integrin-Mediated Delivery and Expression To evaluate one of the possible reasons for Fn-DOTAP-apatite mediated trans-gene delivery and expression we performed an inhibition assay adding excess amount of free (200 μg/mL) fibronectin to the preformed particle suspension, and incubated the cell for the same period of time as followed in usual transfection procedure. Decrease in mRNA transfection potency (Fig. 5B) indicated competitive blocking of the specific integrin receptors by free fibronectin might diminished interaction between Fn-DOTAP-apatite particles with cell membrane thus decreasing uptake and further expression too.

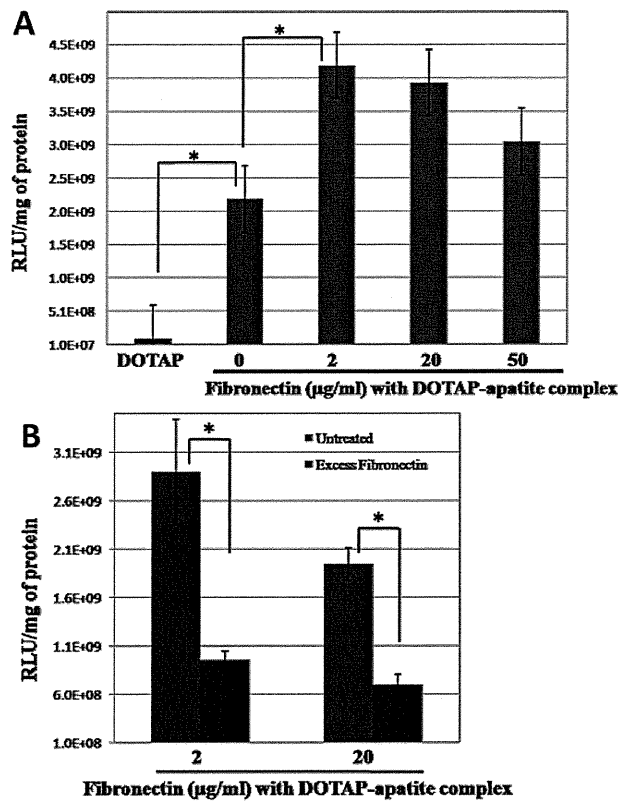

Fig. 5. Gene Expression Pattern by Fibronectin Coated DOTAP-Apatite Particles and Competitive Inhibition Assay

mRNA-DOTAP and fibronectin (2 μg/mL) coated or uncoated mRNA-DOTAP-apatite complexes were prepared as described in the text. Complexes were transferred with 10% FBS to 80% confluent HeLa cells seeded in 24 well plate and incubated for 3 h (A). After the addition of 10% FBS into the complex containing solution, excess fibronectin (200 μg/mL)was added and then the whole solution was added to 80% confluent HeLa cells seeded in 24 well plate (B). Luciferase mRNA expression was measured at 6 h post transfection. Luciferase activity was measured as RLU/mg of protein. * indicates $p<0.05$ *versus* untreated control.

CONCLUSION

Simple fabrication to attain improved tranfection potency is one of the important criteria for designing a better carrier. We could fabricate our developed mRNA carrier with the cell recognizable protein like fibronectin. This is the first time report of inorganic-organic hybrid mRNA carrier by ECM protein. Thus, we have established a superior mRNA transfection methodology based on anchoring liposome bound nano-apatite particles with the ECM protein that possibly could effectively associate with the cell membrane allowing better internalization and subsequent expression.

Acknowledgment This work was supported in parts by Grants-in-Aid for Scientific Research from the Ministry of Education, Culture, Sports, Science and Technology of Japan.

REFERENCES

1) Zou S, Scarfo K, Nantz MH, Hecker JG. Lipid-mediated delivery of RNA is more efficient than delivery of DNA in non-dividing cells. *Int. J. Pharm.*, **389**, 232—243 (2010).
2) Rejman J, Tavernier G, Bavarsad N, Demeester J, De Smedt SC.